Determination of Effective Lifetime and Light Trapping Enhancement in Silicon using Free Carrier Absorption

Determination of Effective Lifetime and Light Trapping Enhancement in Silicon using Free Carrier Absorption

By

Ruslan Khabibrakhmanov

B.Sc.

A Thesis

Submitted to the School of Graduate Studies

in Partial Fulfillment of the Requirements

for the Degree

Master of Applied Science

McMaster University

MASTER OF APPLIED SCIENCE (2021) MCMASTER UNIVERSITY

Department of Engineering Physics Hamilton, Ontario

TITLE: Determination of Effective Lifetime and Light Trapping Enhancement using Free Carrier Absorption

AUTHOR: RUSLAN KHABIBRAKHMANOV, B.Sc., (Saint Petersburg State University, Saint Petersburg, Russia)

SUPERVISOR: Professor Rafael N. Kleiman

NUMBER OF PAGES: X, 100

Abstract

A novel experimental technique has been developed for measuring the light trapping enhancement and the carrier recombination lifetime in silicon wafers. The technique is based on the pump/probe modulated free carrier absorption (MFCA) method, where the probe beam, attenuated by generated free carriers, carries information about the effective lifetime and the average light path enhancement in a textured silicon wafer. For the first time, a reflection mode MFCA technique is presented where the reflected part of the probe beam is used to perform measurements, while the conventional technique is based on measurements of the transmitted part of the probe beam. A theoretical model is presented to explain the behavior of the light beam in double-side polished and double-side textured silicon wafers. The model yields good agreement with the experimental results and explains the difference in the amplitudes of the reflected and transmitted signals. The results of the experimental measurements of the light path enhancement in a double-side textured sample are analyzed and the reasons for their deviation from the Lambertian limit are discussed. This work presents new applications of the MFCA technique and shows how it can be used for the simultaneous determination of more than one crucial characteristic of silicon solar cells.

Acknowledgments

I am grateful for the time I spent at McMaster University, all the knowledge I received, and the new friends I gained. I would like to thank my supervisor, Dr. Rafael Kleiman, for the support and guidance he provided during my study in graduate school. I would also like to thank the entire Kleiman research group and, Shuiawen Gao, David McShannon, and Taz Colangelo in particular, for the support, for their feedback and suggestions during the group meetings, and their help with the experiments. I am grateful that I had a chance to work with Dr. Kevin Boyd, who guided me daily, shared his knowledge, and taught me to work with the experimental setup in the laboratory. I would also like to extend my gratitude to Doris Stevanovic for her assistance and help during experimental work in the CEDT laboratories.

I would like to thank my family, my friends and my significant other for their constant encouragement, love, belief in me, and understanding. I appreciate all of their support through the entire journey of my graduate life.

TABLE OF CONTENTS

List of Figures

List of Tables

1. Introduction

In this work, I demonstrate how the modulated free carrier absorption (MFCA) method can be used in reflection mode geometry to measure the effective lifetime in silicon and analyze the optical properties of the examined sample. I also develop a new experimental technique based on the MFCA method for simultaneous measurement of the light trapping enhancement and effective lifetime in textured silicon samples.

Pump-probe MFCA is a standard method for measuring carrier recombination lifetime in silicon, which is one of the most important parameters to characterize semiconductor material quality. A high lifetime semiconductor material is necessary to achieve superior device performance in high efficiency solar cells or random access memory cicruits [1], [2]. Lifetime measurements provide an opportunity to check the quality of feedstock before device fabrication, ensuring the high quality of the final product. Lifetime screening is particularly important in the photovoltaics industry where there is a trend for less expensive silicon feedstock with lower quality [3], as well as high lifetime material for high efficiency cells [1]. Detailed investigation of the minority carrier lifetime gives information about electrically active defects in a semiconductor material such as their density and energetic location relative to the valence or conduction band edges [4]. The conventional MFCA technique is a transmission mode pump/probe method where the excess carrier density is probed by measuring the free carrier absorption signal following an excitation pulse. An above-bandgap pump beam injects excess carriers into the sample while a below-bandgap probe beam transmitted through the sample is used to monitor the decay of carrier concentration, in either time [5] or frequency [6] domain. The characteristic decay curves – exponential for time domain and Lorentzian for frequency domain – are fit to extract the lifetime. The new approach presented in

this thesis can be described as a reflection mode MFCA technique where the reflected part of the probe beam is used to measure the lifetime. The reflection mode geometry is not new in pump-probe spectroscopy in general. This geometry is used to measure the photomodulated reflectivity and analyze the free carrier dynamics in various semiconductor materials [7]–[9]. In particular, techniques like modulated thermoreflectance (MTR) [10] and photocarrier radiometry (PCR) [11] use a reflection mode geometry to analyze the transport properties of semiconductors. However, the reflection mode technique has not been previously used in free-carrier absorption measurements. The reflection mode MFCA technique can provide a new noncontact and non-destructive approach particularly suited to measure free-carrier lifetime in silicon wafers with potential use in an industrial production line. With this advance, the MFCA method becomes more flexible in the choice of the geometry of the experimental setup.

Modern silicon solar cells have textured surfaces. Surface texturization plays a key role in improving solar cell's efficiency and reducing production costs. A pyramidally textured surface can effectively reduce the reflectance of light on the surface of the cells due to the double bounce effect. The texturing also enhances the light absorption of the weakly absorbed light near the bandgap via multiple reflections inside the cells, thus increasing the cell efficiency [12]. Therefore, control of the quality of the surface during the texturization process in a laboratory or a production line and quality control of the light trapping properties of the final product is an extremely important task. Existing methods of measuring the light trapping capabilities of textured silicon are not suitable for testing in a production line due to high experimental complexity. The method that I develop in this work is relatively simple in implementation. It is based on the pump/probe MFCA technique. It is well known that the FCA signal is proportional to the concentration of excess carriers in the system. But for a textured silicon sample, it is also proportional to the optical

path enhancement factor, as the FCA signal increases due to the longer path of light rays inside a textured wafer. This fact can be used to measure the light path enhancement factor of a textured silicon wafer. For the first time, I present an experimental technique based on pump/probe MFCA that can simultaneously measure the effective lifetime and the light trapping enhancement factor of the textured silicon wafer. I believe this could be an extremely useful technique for the silicon photovoltaic industry as it can evaluate more than one crucial characteristic of a solar cell at the same time.

The content of this work is outlined as follows. In Chapter 2, I discuss the background theory that is relevant to this work. The various absorption and recombination mechanisms in a semiconductor are discussed. The general lifetime measurement procedure is examined, describing the excess carrier density dynamics under optical excitation. The concept of light trapping and maximum light trapping limit are described. In Chapter 3, I review the literature behind lifetime measurement in silicon based on optical techniques, various techniques that use reflection mode geometry, and experimental methods and metrics for measurement of light trapping enhancement. In Chapter 4, I present the experimental apparatus that is used in this work. The components of the experimental setup and the methodology are discussed. The specifications and characterization of the silicon samples used in this work are also presented. In Chapter 5, I develop the reflection mode MFCA technique and compare the experimental results with the transmission mode geometry. Theoretical models describing the light propagation inside double-side polished and textured silicon samples are derived. In Chapter 6, I develop the pump/probe MFCA technique for measurement of the light path enhancement in a textured silicon wafer. I derive a model that describes the measured signal, explains the experimental procedure, and analyzes the results. In Chapter 7, I provide concluding remarks and ideas for future work.

2. Theoretical Background

2.1. Absorption in Semiconductors

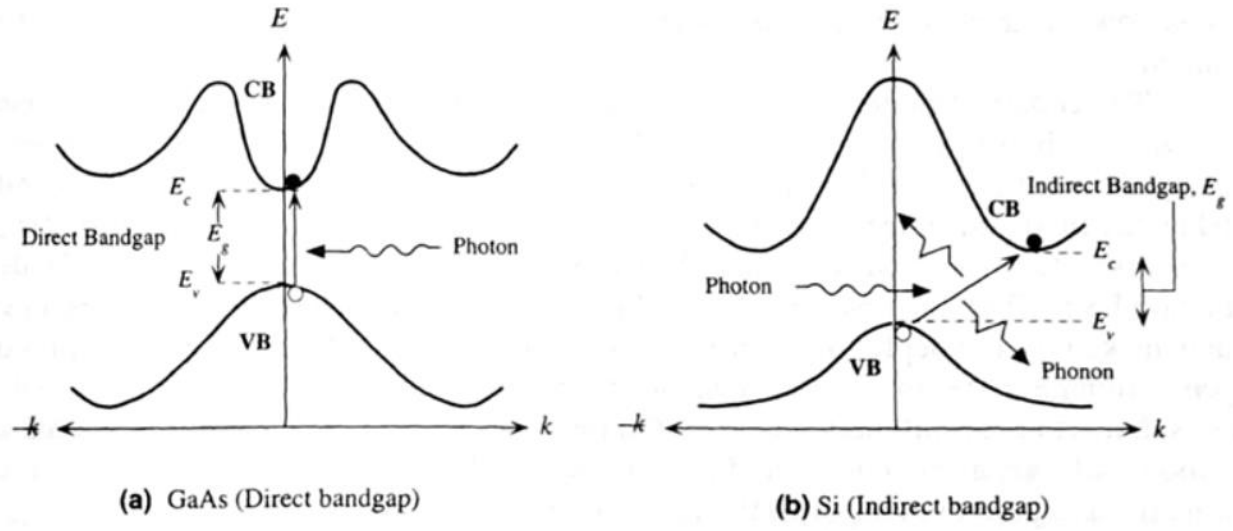

Figure 2.1 Photon absorption in a) direct and b) indirect semiconductor [13].

There are two main absorption mechanisms in semiconductors that are involved in the measurement of effective lifetime: interband and intraband. Interband, or band-to-band absorption, happens when photons with energy higher than the characteristic bandgap of the semiconductor are absorbed to excite electrons from the valence band to the conduction band, leaving holes in the valence band. The mechanism of band-to-band absorption follows the conservation of energy and momentum laws. Therefore, the exact mechanism is different for direct and indirect bandgap semiconductors. In direct bandgap semiconductors, the edges of conduction and valence bands are aligned in crystal momentum space and therefore the absorption process does not require additional momentum. In indirect bandgap semiconductors, as the valence and conduction band edges are not aligned in crystal momentum space, momentum-conserving collision with a phonon is required to promote an electron to the conduction band. The requirement of an additional quasi-

particle to participate in the absorption process reduces the probability of it happening. Thus, in direct bandgap semiconductors, such as GaAs, the absorption coefficient is much higher compared to indirect bandgap semiconductors such as Si. Simplified energy band diagrams for GaAs and Si are shown in Figure 2.1, which illustrates the interband absorption scheme for direct and indirect bandgap semiconductors.

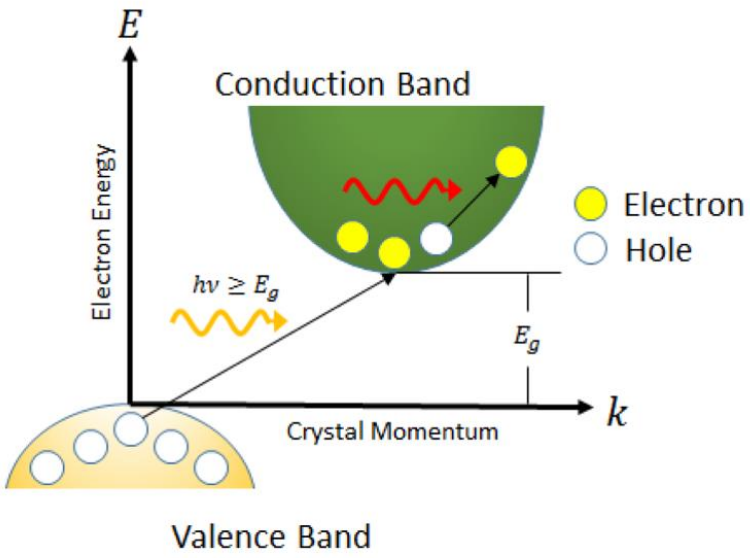

Figure 2.2 Diagram of band-to-band and free carrier absorption in an indirect bandgap semiconductor. [14]

While interband absorption is used to generate electrons and holes in the conduction and valence bands, intraband absorption is used to analyze the concentration of generated carriers. Intraband absorption, or free-carrier absorption (FCA), occurs when a free electron or hole absorbs light and is excited to a higher energy state within the same band. As FCA is proportional to the density of electrons/holes in conduction/valence bands, it gives direct information about the population density of free carriers. A simple scheme of band-to-band and free-carrier absorption processes in Si is shown in Figure 2.2. Due to approximately parabolic energy dispersion in the conduction and valence bands, intraband absorption requires a momentum conserving collision as in the case of interband absorption in indirect bandgap semiconductors. Lattice scattering (emission or

absorption of a phonon), electron-hole scattering, or scattering from a charged impurity can play the role of the momentum-conserving event [15]. The FCA coefficient α_{FCA} is given by the Drude theory of conductivity [16]:

$$\alpha_{FCA} = \frac{q^3\lambda^2}{4\pi^2\varepsilon_0 c^3 n}\left[\frac{n}{m_n^{*2}\mu_n} + \frac{p}{m_p^{*2}\mu_p}\right] \tag{2.1}$$

where q is the fundamental electron charge, λ is the wavelength of light being absorbed, ε_0 is the permittivity of free space, c is the speed of light, n is the refractive index of the semiconductor, m_{n^*} and m_{p^*} are the electron and hole conductivity effective masses, respectively, μ_n and μ_p are the electron and hole mobilities, respectively. In this work, it is considered that free carriers are generated in a one-to-one ratio, therefore $n = p$. Equation (2.1) can be simplified and written in terms of the free carrier absorption cross section σ_{FCA}:

$$\alpha_{FCA} = \sigma_{FCA} n \tag{2.2}$$

In this case, the free carrier absorption coefficient is proportional to the material constant and the free carrier density. However, σ_{FCA}, in general, is also proportional to n as the carrier mobilities depend on the carrier density [17]. The Drude model, which is used to derive Equation (2.1), underestimates the value of σ_{FCA} and cannot correctly explain its behaviour with changing n [18]. This is because the Drude model is based on a more general model that describes FCA only in terms of scattering from acoustic phonons [19]. But other types of particle interaction, such as scattering from optical phonons [20], electron-hole scattering [15], and scattering from ionized impurities [21] can contribute differently to FCA. The type of free carriers in the semiconductor

also has a different impact on σ_{FCA} due to different dominant scattering mechanisms. The change of σ_{FCA} in heavily doped samples is largely due to carrier-lattice scattering [20], while in photo-excited samples it occurs due to carrier-carrier scattering, and arises only for relatively high concentrations [22]. It was shown by Boyd. [14], that when the injected carrier density is small or comparable to the doping level, it can be expected that σ_{FCA} will remain constant.

2.2. Recombination in Semiconductors

Recombination in semiconductors refers to the processes by which electron-hole pairs are lost due to the spontaneous transition of an excited electron from the conduction band to an unoccupied state (hole) in the valence band, in other words, the annihilation of the two carriers. The time-dependant recombination rate of the excess carriers follows an exponential law. The time constant of this exponential decay represents the recombination lifetime – the average time over which the population of carriers above the thermal equilibrium concentration recombine. In general, electron-hole pairs can recombine via different recombination mechanisms: intrinsic and extrinsic. Intrinsic mechanisms are always present and depending on the way the excess energy released by the decay of electron-hole pair is dispersed, two types of recombination are distinguished: radiative and Auger. The extrinsic recombination mechanisms occur indirectly – via a defect center with an intermediate energy level in the bandgap. If the defect center is located in the bulk of the semiconductor, it is the Shockley-Read-Hall (SRH) recombination mechanism, otherwise, it is surface recombination. The total lifetime that is measured – the effective lifetime – is the reciprocal sum of several independent recombination mechanisms:

$$\frac{1}{\tau} = \left[\frac{1}{\tau_{rad}} + \frac{1}{\tau_{Aug}} + \frac{1}{\tau_{SRH}}\right] + \frac{1}{\tau_s} \tag{2.3}$$

where τ_{rad}, τ_{Aug}, τ_{SRH}, and τ_s are the radiative, Auger, Shockley-Read-Hall (SRH), and surface recombination lifetimes, respectively. The dominance of one of these recombination mechanisms is determined by the injection level, the purity, and the type of the given semiconductor. All the recombination mechanisms that occur within the volume of the crystal are separated in the square brackets in Equation (2.3) and represent the bulk lifetime τ_b.

2.2.1. Radiative, Auger and SRH Recombination

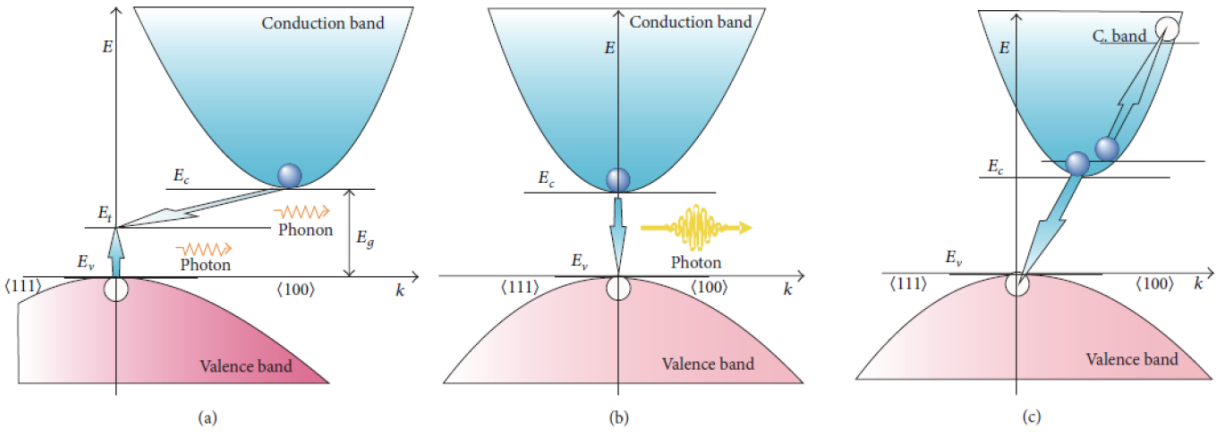

Figure 2.3. Main recombination mechanisms in semiconductors: (a) Trap assisted recombination. (b) Radiative recombination. (c) Auger recombination. [23]

Radiative recombination is the process of direct annihilation of a conduction band electron with a valence hole, involving the emission of a photon with energy approximately equal to that of the bandgap. Radiative recombination is typically the dominant recombination process in direct bandgap semiconductors, as the conduction band minimum and valence band maximum are located at the same position in k-space, so the momentum conservation is ensured. In indirect bandgap semiconductors, such as Si, due to the requirement of interaction with a third quasi-particle to ensure the conservation of momentum, the probability of radiative recombination is reduced and its rate is considerably lower compared to direct semiconductors [4]. The radiative recombination lifetime can be described as:

$$\tau_{rad} = \frac{1}{B(n_0 + p_0 + \Delta n)} \tag{2.4}$$

where n_0 and p_0 are the equilibrium carrier densities, Δn is the density of free carriers, and B is a rate constant.

Auger recombination, shown in Figure 2.3 (c), is a three-particle process where the energy released by the recombination of an electron-hole pair is not emitted with a photon but transferred to a third free carrier. The third carrier absorbs the energy and moves to a higher energy state, after which it quickly releases its excess energy as phonons to the crystal. Due to the requirement of the interaction with a third particle, the Auger recombination lifetime is much longer at lower free carrier densities. However, the probability of recombination occurring will rise at higher carrier densities making the lifetime shorter. The Auger recombination lifetime at high injection levels is given by [4]:

$$\tau_{Aug} = \frac{1}{C_a n^2} \tag{2.5}$$

where n is the free carrier density, and C_a is the so-called ambipolar Auger coefficient. In silicon, Auger recombination becomes the dominant mechanism of recombination at high injection levels.

SRH recombination, or trap assisted recombination, shown in Figure 2.3 (a), is a two-step mechanism where free carriers recombine through the energy states (defect levels) within the forbidden bandgap produced by the presence of impurities or crystallographic dislocations in a semiconductor. A defect level acts as a recombination center – it captures an electron from the conduction band and then a hole from the valence band can be captured to annihilate with the

electron, or the captured electron can relax to the valence band to annihilate a hole. The trap-assisted recombination process requires a change in momentum of the conduction band electron or valence band hole. This momentum change occurs by an interaction with a lattice phonon. The lifetime associated with the SRH recombination is given by the SRH equation [4]:

$$\tau_{SRH} = \frac{\tau_{n0}(p_0 + p_1 + n) + \tau_{p0}(n_0 + n_1 + n)}{n_0 + p_0 + n} \tag{2.6}$$

where n is the density of excess carriers, n_0 and p_0 are the equilibrium carrier densities of electrons and holes, respectively, n_1 and p_1 are the equilibrium densities of electrons and holes when the Fermi level is equal to the defect energy level, and τ_{n0} and τ_{p0} are the capture time constants for electrons and holes which are related to the thermal velocity ν_{th}, the defect concentration N_t, and the capture cross-sections σ_n and σ_p of the specific defect center this way:

$$\tau_{n0} = \frac{1}{N_t \sigma_n \nu_{th}} \tag{2.7}$$

$$\tau_{p0} = \frac{1}{N_t \sigma_p \nu_{th}} \tag{2.8}$$

Analysis of the SRH lifetime is a useful technique for semiconductor characterization as it depends on the energy levels of defects. Often defects are unwanted contaminants that can worsen performance of the system. Measurement of SRH lifetime makes it possible to determine the nature of impurity content.

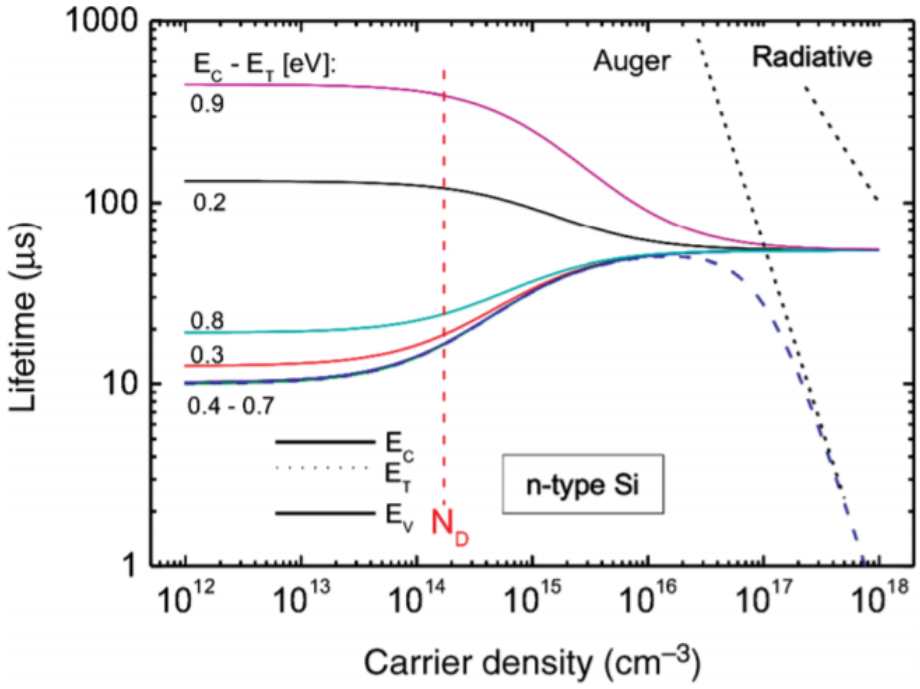

Figure 2.4. The lifetime injection dependence in n-type Si, doped to 10^{15} cm^{-3}, for recombination through traps according to the SRH formalism (solid curves) with trap energy levels as parameters [24].

However, the total effective lifetime strongly depends on the injection level of free carriers. Figure 2.4 presents the injection level dependence of the total effective lifetime as a function of carrier injection, for different energy levels of traps in the bandgap. At low concentrations of excess carriers (values smaller than the doping density N_D shown by red dashed vertical line), the total lifetime in silicon is dominated by SRH lifetime. Low level traps, those which are closer to the conduction or valence band, produce high SRH lifetime. At the same time, deeper traps lead to much lower SRH lifetime as there is a smaller probability for trapped carriers to escape due to thermal excitation. As the injection level rises and becomes higher than the doping level, the SRH lifetimes converge to a constant value independently from the nature of trap levels. Auger recombination becomes dominant, decreasing the total effective lifetime (long-dash line). Radiative recombination is negligible. Typical lifetimes in silicon are in the range of 1 μs – 1 ms.

2.2.2. Surface Recombination and Diffusion

The surface of a silicon wafer represents an abrupt discontinuity in the crystal structure. As a result, the surface is covered with a large number of partially bonded silicon atoms. Dangling bonds act as traps which provide an additional route for free carriers to recombine. So, surface recombination resembles SRH recombination with one major difference that surface defects represent a continuum of energy levels within the bandgap instead of discrete energy levels as in the case of bulk defects. The surface recombination is described by the surface recombination velocity, s and its defining equation is [24]:

$$D\left(\frac{dn}{dx}\right) = -sn \tag{2.9}$$

where D is the diffusion coefficient, and n is the excess carrier concentration.

A high rate of surface recombination, especially in thin samples, can significantly decrease the performance of the device and make it impossible for experimental methods to accurately determine the bulk lifetime. Another source of inaccuracy in lifetime measurements is carrier diffusion produced by high surface recombination. In the case of higher recombination rates at the surface compared to recombination in the bulk, a flow of carriers towards the surface is produced, which leads to the drainage of carriers in the bulk. Thus, the local carrier lifetime is only obtained within the radius of a diffusion length, given by [24]:

$$L_D = \sqrt{D\tau} \tag{2.10}$$

The diffusion length is relatively short for direct bandgap semiconductors, therefore carrier diffusion is not a problem for lifetime measurement techniques. But in indirect bandgap

semiconductors, the diffusion length may be several hundred microns making the surface quality a critical factor for lifetime measurements. Overall, the surface lifetime is described by [24]:

$$\frac{1}{\tau_s} = \frac{1}{d\left(\frac{1}{2s} + \frac{d}{D\pi^2}\right)} \tag{2.11}$$

where d is the smallest dimension of the sample (usually the wafer thickness).

2.3. Measurement of Lifetime

This chapter discusses the theoretical background of excess carrier density dynamics under optical excitation. The theory of carrier distribution is then used to demonstrate how carrier lifetime can be measured in 3 different modes: time, frequency, and quasi-steady-state domains. Most of the theoretical derivations are described in Boyd's work [14] and used as a basis for this work.

A general 3-dimensional equation describing the time dependent excess carrier concentration n in a semiconductor is given by:

$$\frac{\partial n(r,z,t)}{\partial t} = D\nabla^2 n(r,z,t) - \frac{n(r,z,t)}{\tau_b} + g(r,z,t) \tag{2.12}$$

where D is the diffusion coefficient, τ_b is the bulk recombination lifetime, and g is the volumetric generation rate of free carriers. This equation states that the net rate of change of carrier population in a differential volume of semiconductor material is the sum of the net carrier diffusion rate, carrier recombination rate, and carrier generation rate. The generation in this work will always be due to optical excitation. The charge carrier dynamics is fully described in Equation (2.12) without distinguishing between electrons and holes. This is possible because in silicon, in the case when

electrons and holes are generated in equal concentrations, the carrier diffusion is ambipolar [25]. As a result, the carrier diffusion coefficient is intermediate between the values for electrons and holes, and the drift effects may be neglected. A deeper explanation of this effect is given in [14].

In typical lifetime experiments, the examined volume containing free carriers is much smaller than the volume where the carriers are being generated. Thus, it can be assumed that the net rate of carriers diffused out of the examined volume is equal to the net rate of carrier diffused into the volume, and (2.12) can be simplified to a 1-dimension case:

$$\frac{\partial n(z,t)}{\partial t} = D\frac{\partial^2}{\partial z^2}n(z,t) - \frac{n(z,t)}{\tau_b} + g(z,t) \tag{2.13}$$

where z is the dimension along the thickness axis of the wafer. Equation (2.13) can be further simplified in the case when the generation rate is uniform along z, and surface recombination rate can be neglected:

$$\frac{\partial n}{\partial t} = g(t) - \frac{n}{\tau} \tag{2.14}$$

In this equation, the time rate-of-change of free carriers in a semiconductor is described by only the generation rate subtracted by the rate of recombination. In the experiments, n can be measured in the time, frequency, or steady-state regimes. In time-domain experiments, a pulsed laser with narrow pulse width almost instantaneously excites n, and the decay of n back to equilibrium is monitored over time. For a pulse with pulse width $<< \tau$, the generation rate $g(t)$ can be approximated by a Dirac-delta function in time. This transforms the Equation (2.14) to $\frac{\partial n}{\partial t} = -n/\tau$

with the initial condition $n(0) = n_0 = N_0$ where N_0 is the number of photons absorbed from the laser pulse. The solution to this equation is:

$$n = n_0 e^{-\frac{t}{\tau}} \tag{2.15}$$

It can be seen from Equation (2.15), that the lifetime can be calculated by fitting the n decay curve with exponential function parametrized by τ. The decay of carrier concentration is monitored by measuring a physical quantity proportional to it. Depending on the type of experimental technique, different parameters can act as this quantity – the power of reflected microwaves from the semiconductor in the case of μ-PCD technique, which gives information about the change in photoconductivity which is related to n; or the absorption of the optical probe beam in the case of free-carrier pump/probe technique which is directly related to the concentration of free carriers.

In the frequency domain, the generation rate $g(t)$ represents a harmonically varying excitation of angular frequency ω. The modulated g leads to a modulated n. In this experimental regime, the free-carrier population and generation rate can be written in harmonic form: $n=N(\omega)e^{i\omega t}$ and $g(t)=G(\omega)e^{i\omega t}$, where $N(\omega)$ and $G(\omega)$ are the complex amplitudes of the free-carrier population and generation rate, respectively. Substituting n and $g(t)$ into (2.14) and rearranging:

$$N(\omega) = \frac{G(\omega)\tau}{1 + i\omega\tau} \tag{2.16}$$

This is the frequency response of the free-carrier population under a harmonic excitation, which represents a Lorentzian function for a generation rate that is independent of frequency. In a typical frequency domain experiment, the modulation frequency is changed from low to high values and

the complex signal $N(\omega)$ is demodulated on a lock-in amplifier. So, the effective lifetime is extracted by fitting the experimentally found $N(\omega)$ curve with the magnitude of (2.16). It is often more convenient to consider $N(\omega)$ normalized to the generation rate $G(\omega)$. In this case, a generalized lifetime $\mathfrak{T}$ can be defined as:

$$\mathfrak{T} \equiv \frac{N(\omega)}{G(\omega)} = \frac{\tau}{1 + i\omega\tau} \tag{2.17}$$

In quasi-steady state regime, n is measured after excitation with a slowly decreasing generation rate $g(t)$ that ensures constant equilibrium of n with it. This regime can be considered as a special case of Equation (2.15), where $\omega\tau \ll 1$:

$$n = G\tau \tag{2.18}$$

It can be seen from equation (2.18) that under constant generation rate G, the free-carrier population is directly proportional to τ. Therefore, controlling G in an experiment and measuring n, it is possible to extract τ. n, as in the previous regimes, is not measured directly, but related to photoconductivity or free-carrier absorption [26].

As was already stated, Equation (2.14) is a simplified version of Equation (2.12), which was derived taking into consideration several serious assumptions about the properties of a semiconductor. However, an analytic solution to Equation (2.12) is given by Luke and Cheng [27]. Also, Boyd provided an alternative simplified solution which can be used to calculate effective lifetime [14]. In this work, Equation (*2.17*) will be used when performing analyses, as it was shown in [14] that it accurately describes the effective lifetime for various combinations of surface

recombination and absorption coefficients.

2.4. Light Trapping

Light trapping is a mechanism that is used to increase the optical path length of weakly absorbed light in the medium of a semiconductor. A fraction of light that is being absorbed by a semiconductor in a single path is described by Beer's Law:

$$A(\lambda) = 1 - e^{\alpha(\lambda)w} \tag{2.19}$$

where $\alpha(\lambda)$ is the absorption coefficient, and w is the light path which is equal to the thickness of the semiconductor in the case of a single pass. It can be seen that an increase in the optical path length leads to an increase in absorption, which means that more free carriers are generated in the system. This is especially important for silicon solar cells. Due to the lower absorption coefficient compared to direct bandgap semiconductors, silicon solar cells are designed to have higher thickness to absorb enough light. Implementation of light trapping schemes allows thinning silicon solar cells and/or increasing their efficiency. This helps to reduce the cost of cell production by using less silicon but more importantly, it eases requirements for the quality of silicon as the distance that generated carriers would have to travel to get collected is significantly decreased.

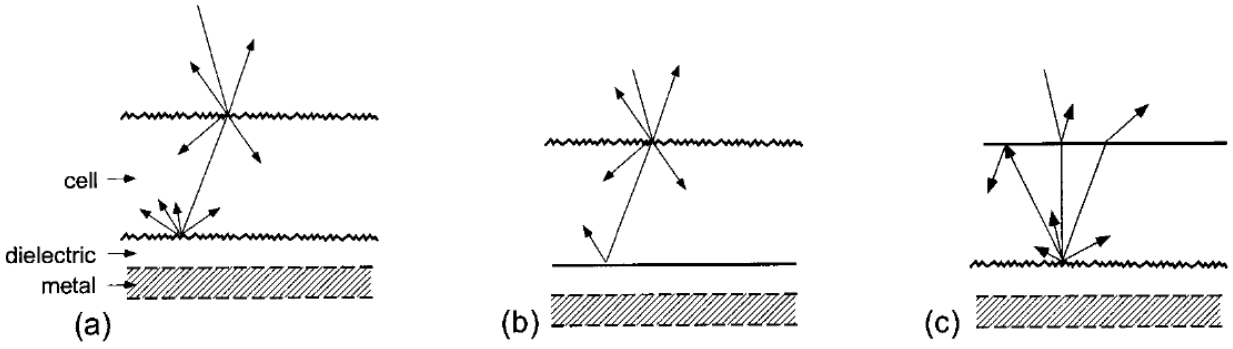

Figure 2.5. Three possible texturing approaches; the rear dielectric/metal reflector combination is optional. [28]

There are several techniques that can be used to achieve light trapping in silicon. One of the most common ways is to texturize either both surfaces of the wafer or just one together with the use of a back surface reflector, as can be seen in Figure 2.5. In this work, a double-side textured wafer is used but without a back metal reflector. Texturing reduces reflection from the surface and causes oblique light paths so the light is trapped by total internal reflection. Only a small fraction of light can escape from the medium after each pass, and the fraction depends on the type of surface that was achieved during texturization. Ideal texturized surface and its maximum theoretical light path enhancement are discussed in the next section.

2.4.1. Lambertian Surface and Yablonovitch Limit

The Lambertian surface reflects and scatters light according to Lambert's cosine law. It is an ideal surface for light trapping, as the light rays become isotropically distributed inside the wafer after the first reflection and completely lose information about their initial direction. So, the light direction inside the wafer is randomized. Using statistical ray optics, it was shown that the intensity enhancement of weakly absorbed light inside an optical medium with respect to its outside is equal to n^2, where n is the refractive index of the medium [29]. It was also derived that the enhancement factor is independent of the source of radiation – it is the same for both isotropic and non-isotropic sources. The intensity enhancement inside the wafer can be further increased by putting a perfect reflector on one of the sides. In this case, light enters the wafer from one of the sides and gets totally reflected at the back side, and the enhancement factor doubles: $2n^2$. Due to the angular randomization of light inside the medium, the absorption enhancement is equal to $4n^2$. Taking into consideration Equation (2.19), absorption enhancement can be interpreted as an enhancement of the average light path L:

$$L \equiv \mu W = 4n^2 W \tag{2.20}$$

where W is the wafer thickness and $\mu = 4n^2$ is the light trapping enhancement factor.

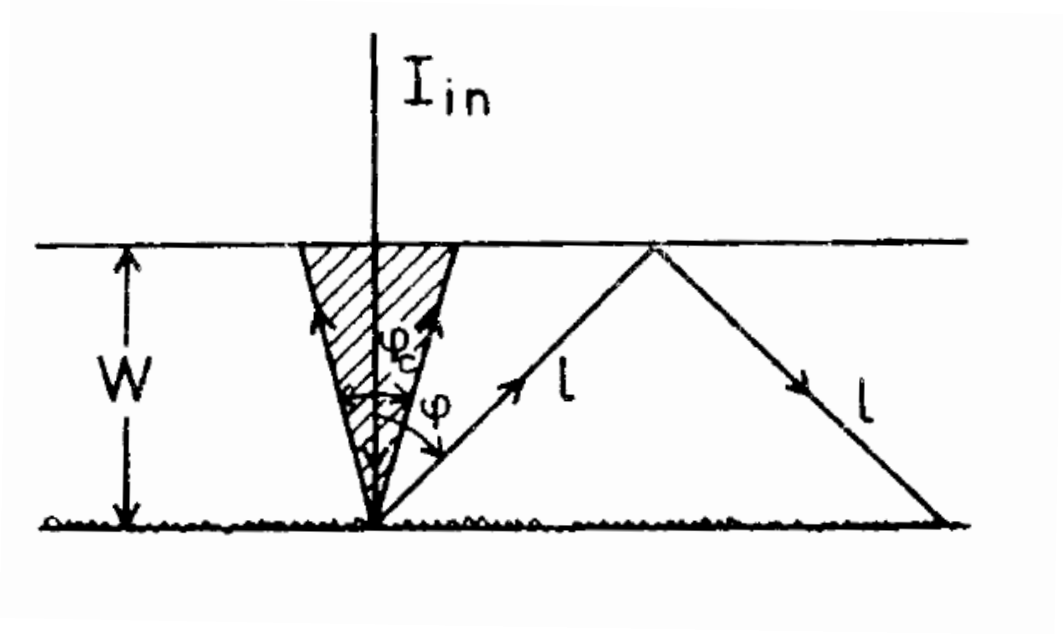

Figure 2.6. Diffuse back reflector leads to loss cone determined by critical angle for total internal reflection θ_c [30].

A different approach to describe optical confinement in silicon solar cells was developed by Goetzberger [30], in which the mean path length of weakly absorbed light was calculated by keeping track of the length of escaping rays. It was shown that the fraction of randomized light intensity escaping from the surface of unity transmissivity is given by:

$$f = \frac{\int_0^{\theta_c} B cos\theta sin\theta d\theta}{\int_0^{\pi/2} B cos\theta sin\theta d\theta} = \frac{1}{n^2} \tag{2.21}$$

where $\theta_c = sin^{-1}(1/n)$, B is the uniform internal brightness produced by the Lambertian surface, and θ is the angle of propagation as shown in Figure 2.6. Eventually, Campbell, in his work [31],

came to the same result, known as the Yablonovitch limit, or the Lambertian limit – maximum light trapping enhancement produced by Lambertian surface with a back surface reflector for weakly absorbed light is equal to $4n^2$. For silicon with a refractive index of 3.5, the enhancement factor is close to 50.

In order to derive a more general expression of enhancement limit for Lambertian surface, it is required to take into consideration the absorption of light inside the medium. In this case, the solution is given in terms of the function G, given by:

$$G = \int_{\theta_c}^{\pi/2} exp(-2\alpha W / cos\,\theta)\, cos\,\theta sin\theta d\theta \qquad (2.22)$$

The function G was evaluated numerically by Goetzberger [30]. Also, an analytical solution was derived by Green [31], who used different approximations for intermediately and strongly absorbed light.

2.4.2. Beyond the Lambertian Limit

In general, the Lambertian surface is not the only light-trapping scheme that can achieve the Lambertian limit. It was shown that the $4n^2$ limit is the average path-length enhancement limit only when averaging over all angles of incidence [32], [33]. Thus, the path length enhancement can be larger than the Lambertian limit for a particular range of incident angles, but at the expense of a smaller path length enhancement at other angles such that the total $4n^2$ limit is not violated. Geometric concentration or angle selectivity schemes can be used to achieve such behavior. In this case, the actual limit of the average path-length enhancement is described by:

$$L = \frac{4n^2W}{sin^2(\theta_{in})} \tag{2.23}$$

where θ_{in} is the acceptance angle of the angular selective filter or the angle associated with the concentration factor [34].

Conventional approaches for light trapping enhancement can be described within principles of geometrical optics. New approaches are shifting towards wave optics targeting a specific wavelength range. Implementation of grating couplers on the surface of thin silicon solar cells is one of the options to reach the light trapping enhancement numbers higher than the Lambertian limit [35]. The main principle behind the grating coupler application in thin solar cells is to produce significant enhancement of the Poynting vector of the electromagnetic radiation of the light inside the cell by coupling the light in a horizontal direction [36]. However, the enhancement is strongly dependent on the incidence angle and wavelength of the light. Absorption enhancement beyond the Lambertian limit can also be achieved by trapping the light into guided modes using nano-particles [37], [38], or photonic crystals [39]. One more approach is to enhance light trapping using localized surface plasmons created by embedding metallic nanoparticles in a dielectric material [40], [41]. Localized surface plasmons produce strong scattering of light at a particular wavelength which depends on the shape, size, and material of nanoparticles [42], [43]. Therefore, it is relatively easy to tune the wavelength of maximum scattering towards the desired wavelength [44].

3. Literature Review

3.1. Carrier Lifetime Characterization Techniques

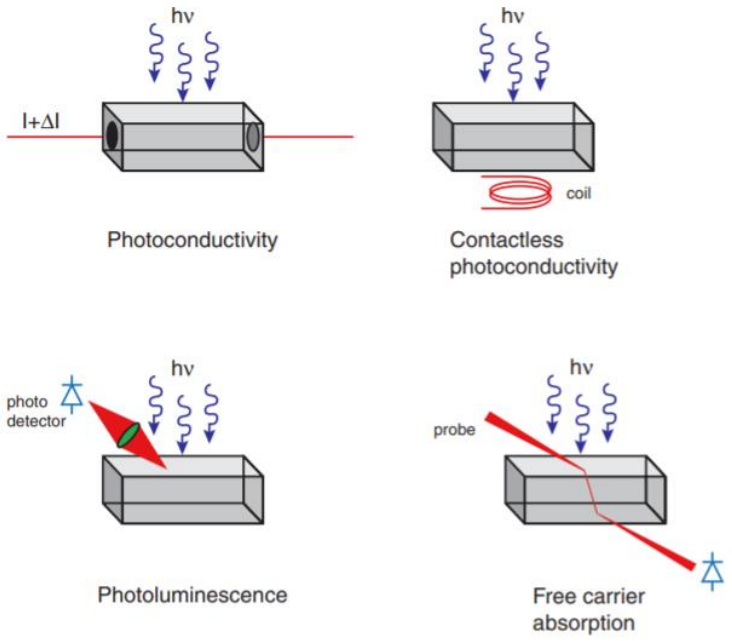

Figure 3.1. Principles of common optical techniques to measure carrier lifetime [24].

Different carrier lifetime measurement methods can be categorized in several ways: either according to physical principles, according to methods used for carrier injection, according to methods used for probing of excess carriers, or according to the operation mode. As the technique which will be described in this work is an optical technique, a short overview of optical methods for lifetime characterizations will be described in this section. All optical techniques, as shown in Figure 3.1, use light to inject free carriers into the system. What makes them different from each other is the way the free carrier population is probed or analyzed and the operation mode. The probing methods will be further discussed in the next chapters. As for the types of operation modes, there are 3 main operation modes: quasi-steady-state, modulation (frequency domain), and

dynamic (time domain). In the quasi-steady-state regime, illumination changes very slowly in time, therefore producing a balance between the generation and the recombination of the electron-hole pair. Thus, an excess concentration of carriers is established in the material. Knowing the generation rate, and measuring the physical quantity connected to the excess carrier concentration, it is possible to calculate the effective lifetime. In the modulation mode, the sample is modulated by a harmonically modulated light source. The modulation frequency is swept from low to high values and the physical quantity which is related to the excess carrier population is monitored. The amplitude and the phase lag between the physical quantity and the modulated light excitation are calculated using a lock-in amplifier. The change in the amplitude and phase with modulation frequency represents the Lorentzian curve that can be fitted to extract the effective lifetime. The dynamic methods are based on measuring the physical quantity after a short excitation pulse. In the simplest case, according to Equation (2.15), the concentration of free carriers experiences an exponential decay after the excitation pulse. By measuring the change of the physical quantity and fitting it with an exponential function it is possible to extract the effective lifetime.

3.1.1. Microwave Photoconductivity

Microwave photoconductivity decay (μ-PCD) is one of the oldest commercial methods used for silicon lifetime characterization [4], [45]. It is based on the change of photoconductivity of a silicon wafer after optical excitation. Due to injected population of free carriers the electrical resistance decreases, and the conductivity increases. In this technique, the semiconductor is placed inside of a microwave cavity and the microwaves are brought incident upon the semiconductor. A pulsed laser with a pulse width much less than the effective lifetime of the sample increases the photoconductivity of the sample, which causes the wafer to become more metallic and more reflective to the microwaves. After illumination, the microwave reflectance decays back to

equilibrium as the photoconductivity returns back to initial values. The recombination constant is extracted by monitoring the change in reflectance with time and calculating the decay constant.

The change in reflectivity of microwave power is linearly proportional to the change in photoconductivity only for low injection levels [4]. At higher injection levels the microwave reflectivity becomes a highly non-linear function of photoconductivity [46]. Therefore, this method brings some significant complications for lifetime measurement over a wide range of injection levels. In order to perform a measurement at high injection levels, a bias lamp is used to set a steady-state carrier concentration above the equilibrium level. The pump laser then produces a small perturbation of excess carrier concentration. In this way, the linearity between the reflected microwave power and the photoconductivity is conserved, and the lifetime can be calculated for large carrier concentrations.

3.1.2. Radio Frequency Quasi-Steady State Photoconductance

One more lifetime measurement technique that uses the principle of photoconductance is the radio frequency quasi-steady state photoconductance (RF QSSPC) [47], [48]. In this technique, the absolute amplitude of photoconductance is measured under quasi-steady state illumination. The excitation source is usually a flash lamp with a slowly decaying power, slower than the lifetime of the sample. Under this operation regime, the wafer's excess carrier population is always in equilibrium with the excitation. Therefore, this technique allows obtaining the photoconductance under a wide range of illumination intensities. In order to measure the photoconductance an RF bridge is coupled inductively to the sample with a conductive coil [4]. The alternating magnetic field in the coil induces eddy currents in the wafer, which produces loss of energy proportional to the photoconductivity. The signal proportional to the photoconductivity is observed on a digital

oscilloscope. However, a reference cell is required to accurately determine the time dependence of the excess photoconductance of the sample and the illumination of the flash lamp by using appropriate calibration functions.

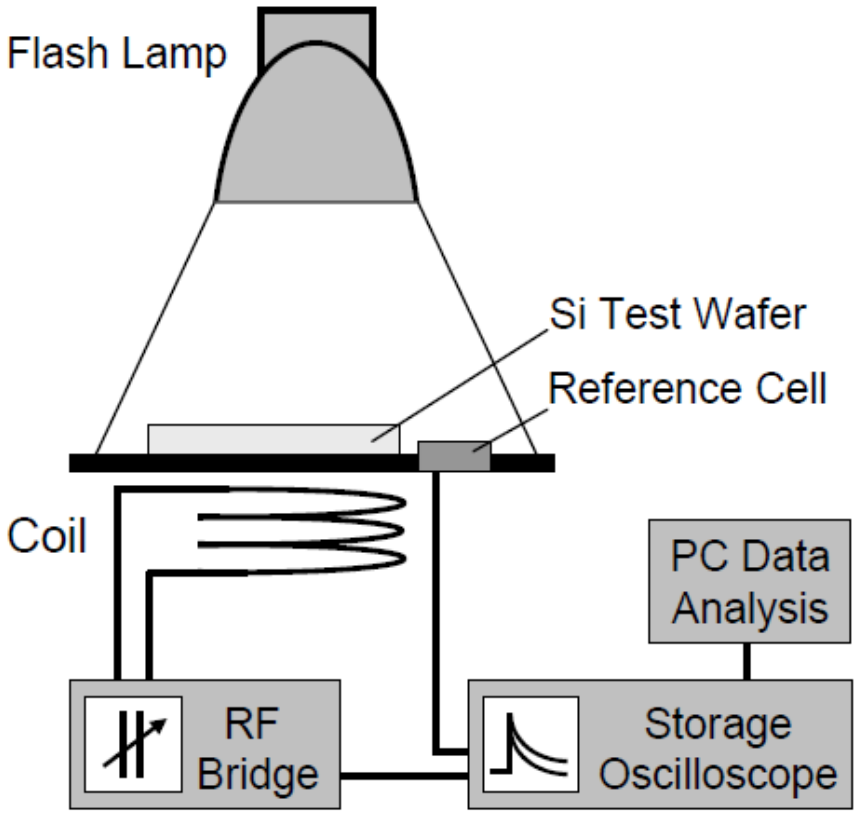

Figure 3.2. Schematic diagram of the inductively-coupled photoconductance apparatus [4].

The QSSPC technique can be used to measure the effective lifetime in the range between 0.1 μ*s* to several milliseconds over a large range of injection levels from 10^{12} to 10^{17} cm^{-3} [4]. Thus, this is a great method to analyze the dependence of lifetime on injection level.

3.1.3. Photoluminescence

The photoluminescence (PL) method is only applicable for semiconductors experiencing radiative recombination. Even though the radiative recombination rate is low in indirect bandgap semiconductors, PL still can be used to extract their lifetime due to the high sensitivity of the technique [24]. Most commonly, PL is used in the QSS regime and is therefore called QSSPL. This method is based on simultaneous measurement of both the oscillating optical irradiation and the corresponding photoluminescence intensity as a function of time [49]. The timescale of the excitation modulation must be much greater than the effective lifetime of the sample. The effective minority carrier lifetime is then extracted from the time shift between maxima of irradiation intensity and photoluminescence intensity [50]. Even though this method has high sensitivity, sophisticated calibration of the system is required to extract accurate effective lifetime [51].

3.1.4. Free-Carrier Absorption

Free-carrier absorption (FCA) is directly proportional to the free carrier population, therefore it can be used as a physical quantity for lifetime measurement. In general, an experimental setup used in this technique consists of pump and probe light sources. An above-bandgap pump beam injects excess carriers in the sample while a below-bandgap probe beam transmitted through the sample is used to monitor the decay of carrier concentration, in either the time [5] or frequency domain [6]. The characteristic decay curves – exponential for time domain and Lorentzian for frequency domain – are fit to extract the lifetime. Typically, the pump beam radius is much larger than the probe beam radius. This is done to achieve uniform carrier density in the area of examination.

Frequency domain FCA is the main experimental technique used in this work. It is also called

modulated free-carrier absorption (MFCA). The frequency domain approach was used in one of the earliest FCA work which was the first step towards the modern MFCA technique. Huldt used a tungsten strip lamp as the pump source, and a monochromator set to emit light with a wavenumber of 900 cm^{-1} [52]. Modulation of the pump was performed by a mechanical chopper. He showed that the lifetime of a near-intrinsic germanium sample can be measured by sweeping the modulation frequency of the pump and monitoring the change in the intensity of the transmitted probe. Nilsson then demonstrated an improved version of Huldt's technique, where the probe beam was also modulated to improve the sensitivity of the system [53]. One of the first modern versions of the MFCA technique was presented by Sanii et. al [54]. In their work, a He-Ne laser with 632 nm wavelength is used as the pump, and a second He-Ne laser emitting at 3.39 μm is used as the probe. The pump is modulated by an electro-optic modulator and the probe is detected with an InAs photodiode. Most of the modern MFCA techniques share the same principles presented in [54]. There is a great number of different versions of the MFCA technique, for example, the single beam MFCA technique was developed in Dr. Kleiman's lab [55].

3.2. Reflection Mode Techniques

There are several pump/probe techniques that use reflection mode geometry to analyze the optical properties of a semiconductor. Most of them measure the modulation of the reflection coefficient induced by the modulated pump beam. There is a discrepancy in the naming of these techniques in literature. In general, all of them can be called as photomodulated reflectance (PR or PMR) [56]. But the change in reflectance can be caused by different physical phenomena. Thus, PR techniques are distinguished by some authors depending on the dominant physical effect. Techniques, where

the change in reflectance is caused by thermal effects (temperature modulation of the sample due to absorption of the pump beam), are called the photomodulated thermoreflectance (PTR) [10]. Another contribution to the reflectance modulation arises from a free carrier Drude effect on the optical refractive index [10]. There is also the photoreflectance effect, which can be monitored when the optically induced modulation of the surface built-in electric field causes reflectance modulation via the Franz-Keldysh mechanism [56]. One more technique that measures the change in the refractive index of a semiconductor is photocarrier radiometry [11].

Usage of reflection geometry for MFCA measurements does not provide specific benefits other than an additional degree of freedom for the experimental setup. It does not measure the change in refractive index and only concentrates on FCA. Reflection mode geometry can be useful in specific scenarios, for example when testing the quality of silicon samples on a production line.

The reflection mode MFCA was previously mentioned in Petursson's work [57], but it does not provide the analysis of light propagation inside a silicon sample and how it can affect the experimental results.

3.3. Measurement of Light Trapping Enhancement

Texturization of the silicon solar cell surface significantly improves its performance. Therefore, the quality of the texturized surface should be monitored to control the quality of texturization. In addition, information about the surface quality allows comparing different texturization approaches and different solar cells with each other. Some common techniques used to monitor the quality of the surface are angle-resolved optical reflectance [58] and scanning electron microscopy [59]. However, these techniques do not provide full information about the light

trapping properties of examined wafers. SEM only gives a visual picture of the surface, and reflectance techniques include assessment of reflection quality of the surface and parasitic absorption, making it difficult to distinguish light trapping properties of the system. Moreover, the abovementioned techniques do not allow scientists to quantitatively compare various light trapping structures with each other. In this chapter, I present a short review of different approaches used for assessing light trapping enhancement and several experimental techniques that are based on them.

3.3.1. Light Trapping Metrics

There are several approaches to quantify a solar cell's light trapping. Each has pluses and minuses. One of the most popular ways is to assess the quality of light trapping by its effect on carrier generation as a function of wavelength, in other words by absorption spectrum [60]. Comparison of band-to-band absorption between textured and polished solar cells provides direct information about the light trapping quality of the textured cell. However, this method has several major drawbacks. Absorption spectra of different cells have to be compared graphically since they do not provide quantitative assessment of the surface quality. Moreover, absorption strongly depends on the thickness of a cell, therefore it is impossible to compare different types of cells between each other. Lastly, various sources of parasitic absorption could negatively affect the assessment of light trapping quality of solar cells. The absorption spectrum can be determined by various experimental techniques, ray tracing, or theoretical calculations.

Another simple metric to define the quality of light trapping is the increase in the current it induces [60]. A short circuit current generated in a textured cell is compared to the short circuit current generated by a similar cell but without light trapping structure. The generated current can be measured experimentally measuring actual I-V characteristics of the solar cell, or it can be

determined by measuring the absorption spectrum of the cell and converting it into the generated short circuit current. The advantages of these metrics are that it is represented by a single value instead of a graphical spectrum, and the value is directly related to cell performance. The drawback of this method is that cells with different thicknesses can not be compared with each other. A different metric that also relies on the measurement of the short circuit is the Light Trapping Efficiency (LTE) calculation [61]. This method compares the total current gain achieved by the real examined structure to the theoretical maximum current gain of the ideal Lambertian scatterer. This metric can be used to compare cells with different thicknesses. Figure 3.3 presents a comparison of the LTE of different Si structures from literature. It is important to notice that experimental results show significantly lower LTE numbers compared to numerical studies.

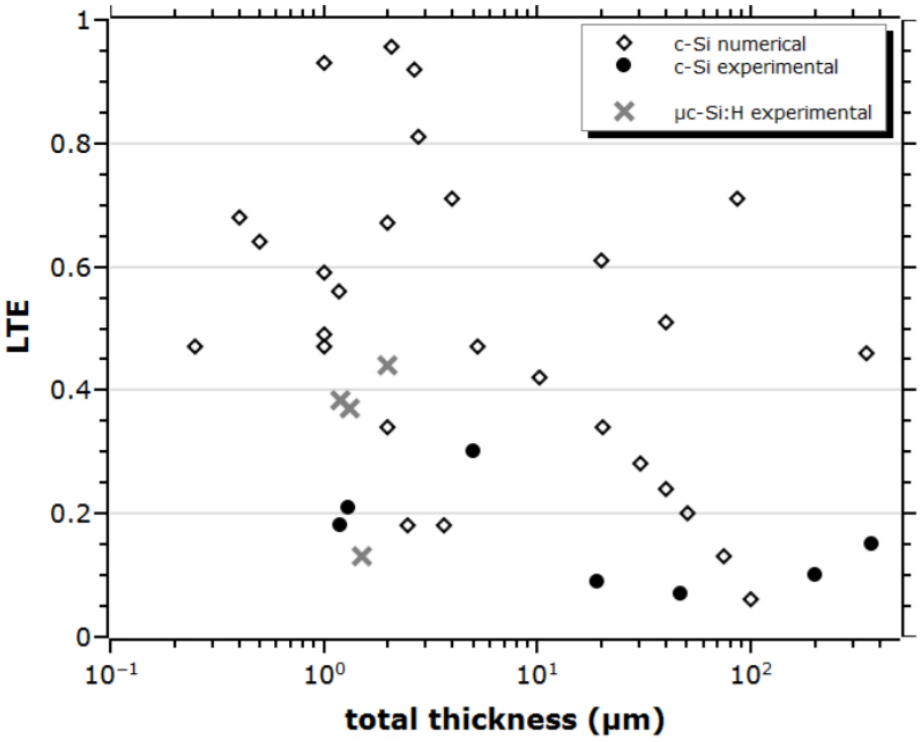

Figure 3.3. The calculated light trapping efficiency (LTE) of various Si structures in literature [61].

Effective light pathlength enhancement (Z) is one more metric used to assess the light trapping

quality of the cell. It gives information about the average length of the optical path of the light rays inside the textured wafer [60]. In other words, it describes the solar cell's optical thickness relative to its actual thickness. The effective pathlength is usually calculated from the absorption spectrum [62]. Similar to the short circuit metrics this method gives a single value of Z. But Z depends on the wavelength of the incident light, which means that comparisons between cells must be graphed. It can be useful to measure Z for low-absorption limit, where Z is independent of cell thickness and incident wavelength.

3.3.2. Experimental and Theoretical Techniques

Theoretical and experimental techniques measure particular physical quantities which are then used to assess the light trapping enhancement factor with one or another metric mentioned in the previous section. They are divided into four groups based on the physical quantity they measure: measurement of generation current, absorption, estimation of light path enhancement, and simulations. A short description of some of these experimental and theoretical techniques is given below.

Direct measurement of the generation current of the solar cell under illumination is the most straightforward way to assess the quality of light trapping surface [60]. However, this technique requires the assembly of a full solar cell and cannot be used to control the surface quality during the texturization process when the solar cell is not assembled.

As several metrics rely on the measurement of the absorption spectrum, there are several techniques to measure it. One of the most popular techniques is to measure the reflectance spectrum of a cell or a wafer, placed in an integrating sphere with a perfect back reflector, using a spectrophotometer [29], [62]. The reflection spectrum is then converted to the absorption spectrum

and used in one of the metrics. This technique has several drawbacks. First, it does not provide information about the origin of absorption. Increased absorption could be monitored due to an actual increase in the optical path length or due to lower reflectance of the surface. The second problem is connected to the first one – for incident light with wavelengths above 1000 nm parasitic effects, like FCA, start to play a significant role. As a result, the absorption spectrum may overestimate the light trapping enhancement which is connected only to band-to-band absorption. To overcome this problem, the spectral luminescence technique can be used in combination with reflectance measurements [63]. This technique measures the photoluminescence spectrum of a silicon cell for wavelengths that could cause considerable FCA. Spectral photoluminescence intensity is proportional to band-to-band absorptivity and independent from FCA. One of the major issues of the photoluminescence technique is relatively low intensity of silicon photoluminescence. Therefore, it requires a highly sensitive liquid nitrogen cooled detector. Also, it is problematic to use this technique in a production line for monitoring the quality of a texturized surface in situ, as it requires the usage of an integrating sphere to collect all emitted light.

One of the rarely used techniques is Raman spectroscopy. It relies on the fact that the number of generated Raman photons in a thin film solar cell is directly proportional to the optical thickness of the cell [64]. Therefore, relative changes of the Raman signal can be used to compare the light trapping capability of different cells.

Theoretical estimation of light trapping enhancement is a wide field of research that includes various methods. Most of them can be divided into two parts: based on analytical solutions and based on ray tracing simulations. One of the first analytical calculations of light trapping properties of different types of textures was presented by Campbell [31]. He calculated the percentage of incident rays remaining trapped as a function of the number of passes made through substrates

with structured top and rear surfaces. This is also an example of an unusual metric not mentioned in the previous section. The ray tracing simulations can estimate the average path length of propagated rays and the absorption spectrum of a textured structure. One of the latest remarkable works was published by Manzoor et. al [34]. They use different techniques such as atomic force microscopy and angle resolved reflectance to create a map of the textured silicon surface. There are different types of textures like inverted pyramids and random pyramids. Analyzing the angular distribution function of rays propagating inside silicon samples, they estimated the total pathlength enhancement limits of different surface structures and compared them with an ideal Lambertian scatterer.

In this work, I will present a new technique based on pump/probe MFCA. This technique has not been shown in literature before.

4. Experimental

4.1. Overview

The experimental setup in this work represents a generic pump/probe configuration for performing lifetime measurements. A laser with 1064 nm wavelength is used as a pump beam as its energy is higher than the silicon bandgap and can be used to generate free carriers, but at the same time, its energy is low enough to provide relatively homogeneous axial illumination throughout the probing volume. The probe beam has to be weakly absorbed by silicon, therefore a 1550 nm laser is chosen as its energy is below the bandgap of silicon. The probe beam is mostly absorbed by intraband free carrier absorption. The experimental setup can be divided into three separate parts: pump, probe, and measurement branches. Pump and probe branches are almost identical to the ones used by Boyd in his dissertation [14], and they are described in this section. The measurement branch is modified and is different for experiments with different types of samples. It will be discussed in the next section.

Figure 4.1 shows the pump branch of the experimental apparatus, with a red line denoting the path of the laser. It consists of the pump laser source, modulation components, and components that control the power and the size of the beam. A Laser Quantum Opus laser is used for the pump. It emits horizontally polarized light and can produce up to 10 W of optical power. In the experiments, the laser's operating power is set to 2 W. The pump beam is modulated by a custom Conoptics electro-optic modulator (EOM) which is driven by a Conoptics Model 25 A Driver, capable of introducing an analog signal onto the laser beam at frequencies ranging from DC to 25 MHz. A Zurich multi-frequency lock-in (MLFI) amplifier is used to supply a sinusoidal drive signal to the

modulator. After passing through the EOM, the laser beam passes through a half-waveplate/polarizer pair, which is used to control the laser power. The polarizer is mounted to the motorized rotational stage which is connected to a computer and controlled remotely. After emerging from the waveplate/polarizer pair, the laser beam is guided through a Standa beam expander. After that, the laser is guided to the sample.

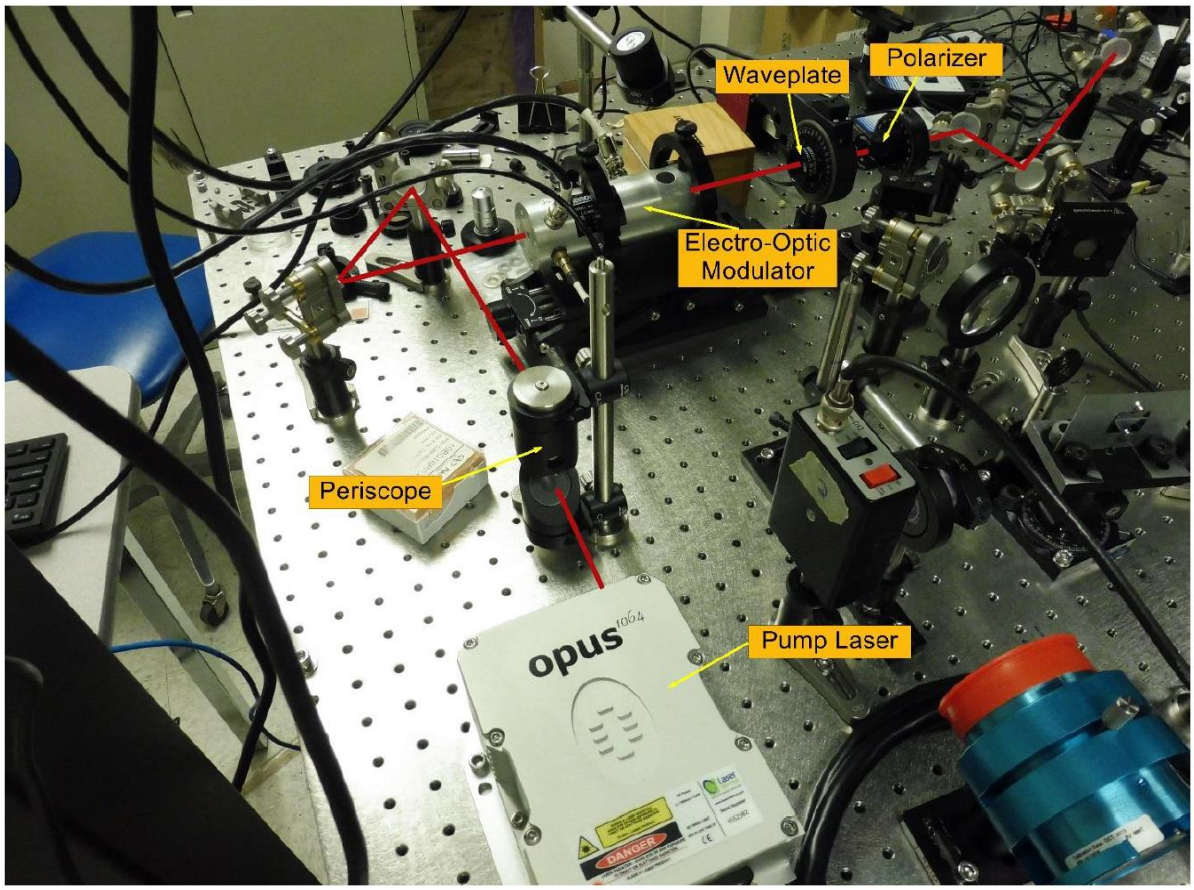

Figure 4.1. Annotated photograph of the pump branch of the experimental setup [14].

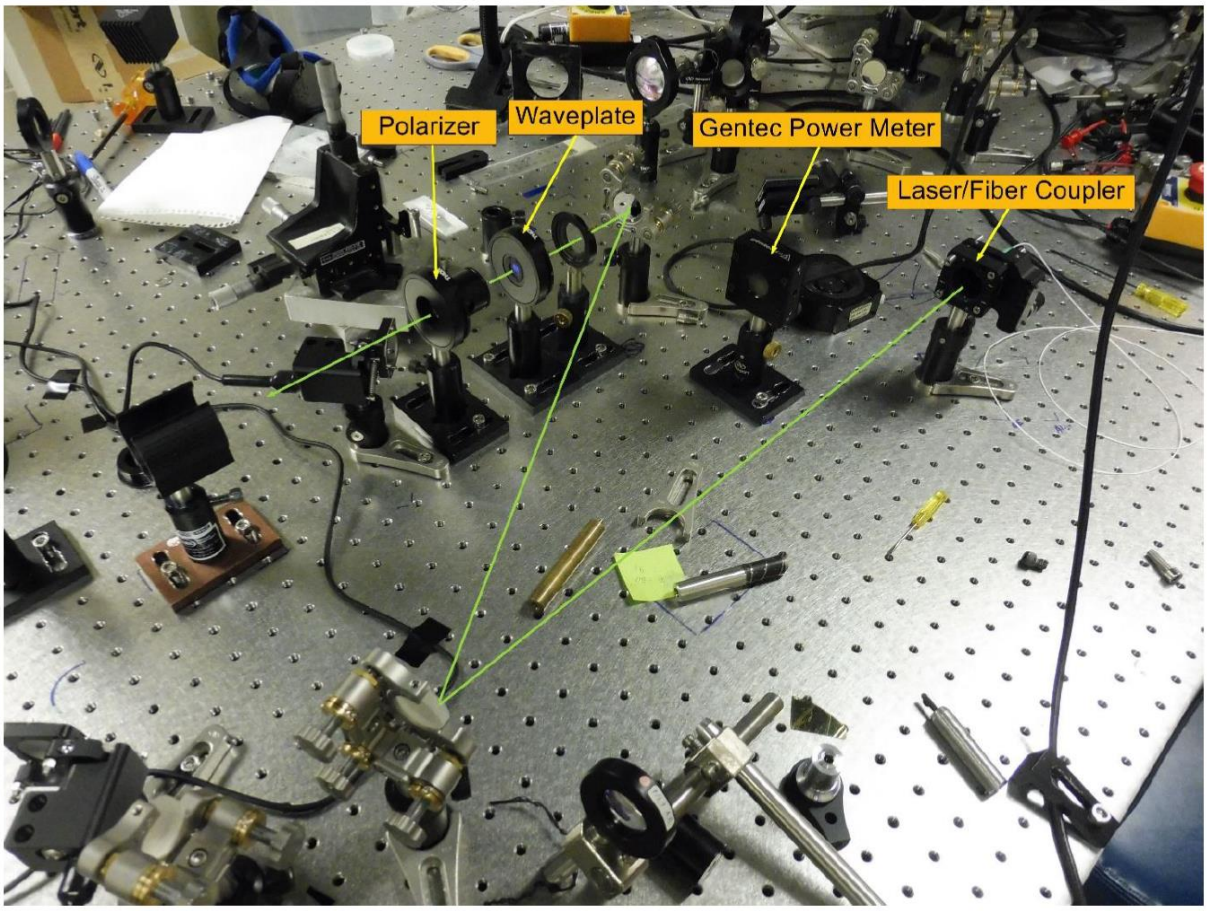

Figure 4.2. Annotated photograph of the probe branch of the experimental setup [14].

Figure 4.2 shows the probe branch of the experimental apparatus, with a green line denoting the path of the probe laser. The probe laser is a Thorlabs FPL1009S fiber optics laser emitting at 1550 nm. The laser is driven by an LDC205C current source set to 250 mA, providing about 55 mW of optical power. A fiber coupler collimates the probe beam upon exiting the fiber. A half-waveplate/polarizer pair is used to control the power of the probe beam. After emerging from the waveplate/polarizer pair, the probe beam is guided through an additional half-waveplate mounted to the motorized rotational stage. The purpose of this component is to control the polarization of the probe beam, as it will be needed to investigate the impact of polarization on the FCA signal.

4.2. Experimental procedure

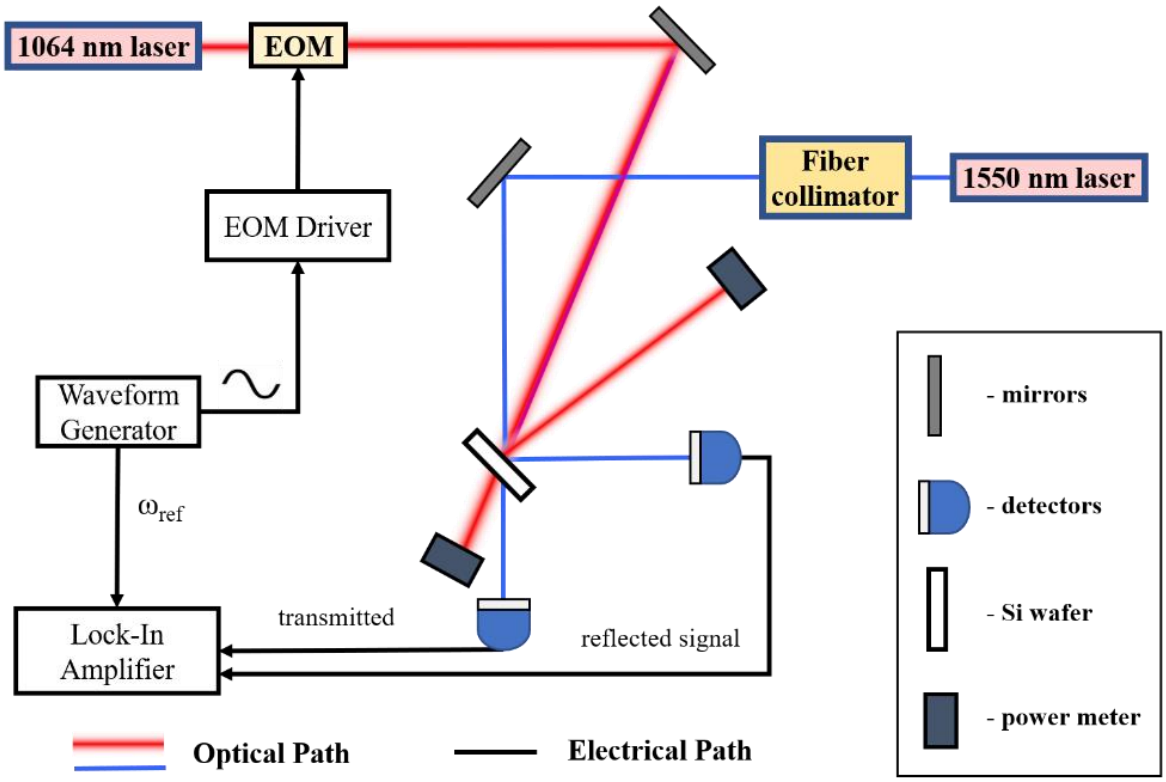

Figure 4.3. Approximate block diagram of the experimental setup.

In this work, two types of measurements are done: measurement of the effective lifetime in polished samples and in textured samples. Both types of measurements use similar experimental methodology. The main practical difference is in the way the probe beam is collected. Figure 4.3 presents a general scheme of the experiment which is valid for measurements with both polished and textured samples neglecting some minor details. The pump and probe beams illuminate the sample on the same side. In the experiment with a polished sample, the angle of incidence is approximately 20 and 45 degrees from normal for the pump and probe beams, respectively. The power of the pump beam is set to 750 mW.

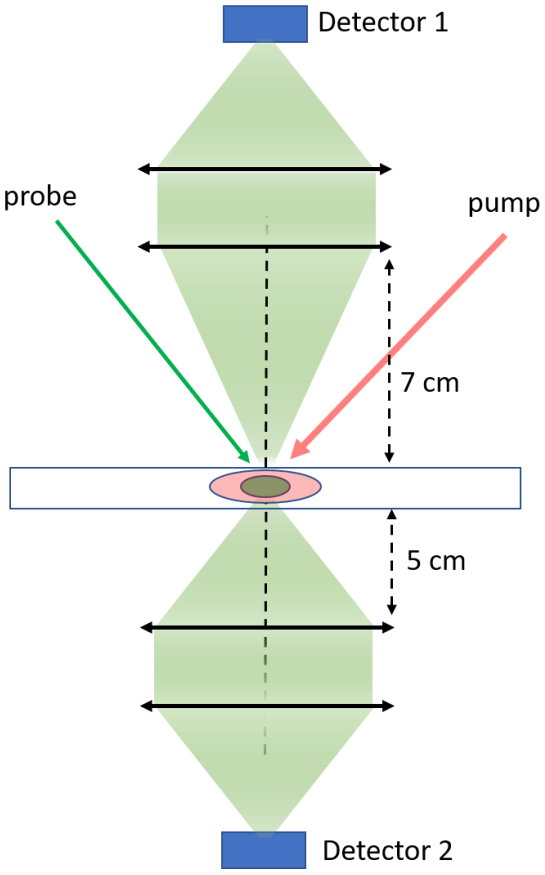

Figure 4.4. Block scheme representing the experimental setup used for collecting the reflected and transmitted diffused probe beam.

In the experiment with a textured sample, the angles of incidence of the probe and pump beam are 30 and 37 degrees from normal, respectively. Figure 4.4 presents an approximate scheme of the setup designed to conduct experiments with the textured sample. The reflected and transmitted parts of the probe beam become diffuse after interaction with a textured sample. Therefore, a set of pairs of lenses is used to collect the maximal amount of light and focus on the detectors. Due to the specifics of the optical setup on the test bench, the set of lenses used to collect reflected light is placed 7 cm away from the sample, while the set used for transmitted light is placed only 5 cm away. This introduces a difference in the amplitude of the detected signal as more transmitted light

is collected than reflected light. The difference is compensated mathematically in the analysis procedure and will be discussed in the next chapters.

In order to ensure that the probe beam is measuring the lifetime in a uniformly injected region, the pump beam is expanded to a diameter of 3 mm, and the probe beam is focused to a diameter of 50 μm. After reaching the surface of the sample, the probe beam separates into reflected and transmitted parts. The transmitted beam is also collected in order to validate the results of the experiment in the reflection mode. Both transmitted and reflected probe beams are focused into two separate New Focus Model 2033 Germanium photodetectors set to 2000 × gain, which have a bandwidth of 200 kHz at this gain. In the experiment with a textured sample, the diffuse reflected and transmitted radiation is collected and focused into photodetectors using a set of lenses with a wide diameter. The AC and DC components of the detector signals are measured in the Zurich MFLI. The power of the incident, transmitted, and reflected pump beams is measured using Gentec calibrated power meters in order to determine the absorption and reflection coefficients of the sample. The modulation frequency is changed from 100 Hz to 100 kHz, in 50 logarithmically spaced steps, and the amplitude and phase of the FCA signal are measured at each step.

The experimental setup is almost fully automated. It is controlled through an Application Programming Interface (API) developed by Boyd and customized and improved for particular experiments by me. The API is written in the Python programming language.

4.3. Sample Specifications and Characterization

4.3.1. Sample Specifications

Table 1. Specifications of silicon wafers used in this study.

Wafer ID	**Thickness (μm)**	**Resistivity (Ω cm)**	**Doping Density (cm^{-3})**	**Surface Coating**	**Surface Type**	**Growth Type**
Thick	1470 ± 2	1 - 5	$4.51x10^{14}$	Native Oxide	Double-side polished	CZ
El-Cat_2_9	325 ± 2	1 - 10	$3.2x10^{15}$	Thermal Oxide (100nm)	Double-side polished	FZ
Undoped	575 ± 2	3000	$1.5x10^{12}$	Native Oxide	Double-side polished	FZ
El-Cat_15_1	325 ± 2	1 - 10	$3.2x10^{15}$	Native Oxide	Double-side polished	FZ
El-Cat_15_2	325 ± 2	1 - 10	$3.2x10^{15}$	Native Oxide	Double-side textured	FZ

Table 1 shows the specifications of all the silicon wafers used in this work. The Thick wafer is Czochralski (CZ) grown while the other wafers are all Float Zone (FZ) grown. One of the wafers, El-Cat_15_2, is double-side textured and was used in the study of light trapping enhancement. The other wafers are all double-side polished. All of the doped wafers are n-type phosphorus doped.

4.3.2. Texturization and Characterization

In this section, I will describe the texturization procedure and analysis of the achieved surface. Prior to texturization, the sample was cleaned by dipping into a piranha solution (1 part H_2O_2, 4 parts H_2SO_4) for 5 minutes and then deionized (DI) water rinsed for another 5 minutes. After that, the sample was dipped into an HF solution (1 part HF, 10 parts DI water) for 5 minutes and then rinsed in DI water for 5 minutes. After cleaning, the sample was textured by anisotropic etching in a weak solution of KOH with isopropyl alcohol (1g KOH, 5 ml isopropyl alcohol, 125 ml DI water) at 70 °C for 10 minutes. The solution was constantly stirred during the etching procedure. This etching recipe was chosen because it showed good experimental results in literature creating a surface with uniform distribution of random pyramids [12].

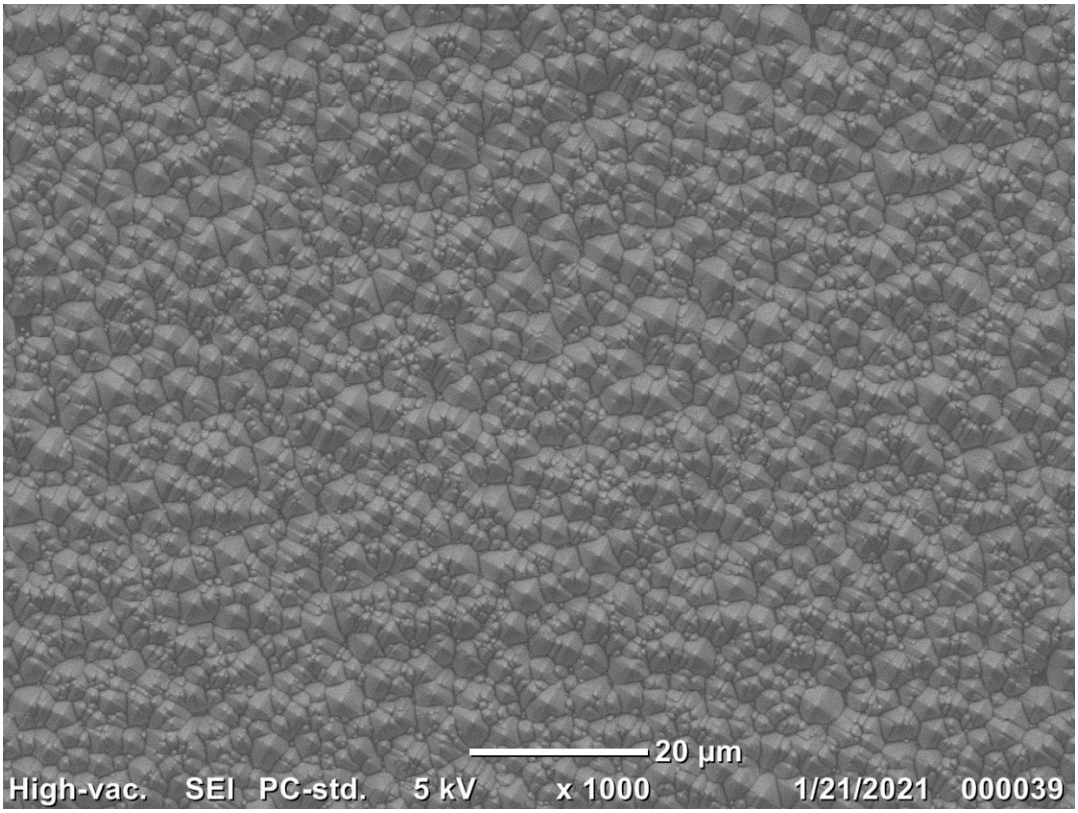

Figure 4.5. SEM image of the textured sample (x1000 magnification).

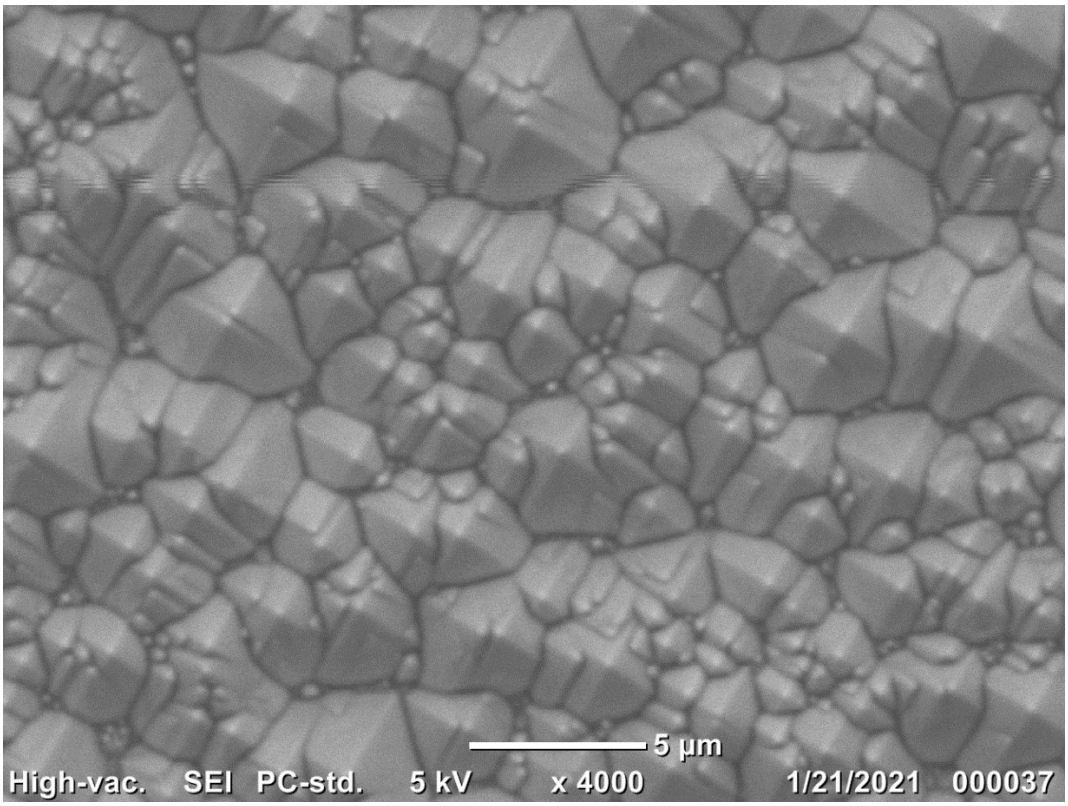

Figure 4.6. SEM image of the textured sample (x4000 magnification).

Figure 4.3 and Figure 4.5 present scanning electron microscopy (SEM) images of the textured sample with different magnification rates. It can be seen that the achieved surface consists of randomly distributed pyramids with sizes of individual pyramids varying from less than 1 µm to 4-5 µm.

5. Lifetime Measurement in Reflection and Transmission Modes

5.1. Overview

In this chapter, I present the results of the MFCA experiment in the reflection and transmission modes. A theoretical model is developed to analyze and explain the behavior of light experiencing multiple reflections inside the sample. Experimental verification of the model is also provided in the next sections. Additional considerations that must be taken into account in these experiments are discussed in the last section of this chapter.

5.2. Experimental Results

The experimental procedure is nearly identical for double-side polished and double-side textured samples. The only difference is in the way the signal is acquired from the textured sample. The textured sample makes the reflected and transmitted parts of the initial light diffuse in a nearly Lambertian way. Therefore, diffuse light from the textured surface must be collected with the help of the system of lenses. This introduces a difference in the way the final results are analyzed for polished and textured samples. Thus, in the next section, the experimental results are given separately for these two types of examined samples.

In the experiment, a harmonically modulated pump beam at an angular frequency ω generates a time-dependent concentration of excess carriers in the sample with the density:

$$\Delta n = \Delta n_0 + \Delta n_1 e^{i\omega t} \tag{5.1}$$

where Δn_0 is the mean excess carrier density induced by the pump laser and Δn_1 is the magnitude of the AC amplitude of the excess carrier density. The change in the modulated excess carrier density is observed versus modulation frequency. The effective recombination lifetime can be calculated by fitting the real or imaginary part of the FCA signal with the corresponding part of Equation (2.17).

The various bulk and surface mechanisms that affect the lifetime, as well as methods to increase it such as surface passivation, do not significantly impact the measurement of lifetime values and are not considered further in this work. Equation (2.17) presumes a laterally uniform carrier distribution, which is ensured by experimentally imposing the requirement that the pump beam is much larger in diameter than the probe beam. Strict axial uniformity of the carrier distribution is not required since Equation (2.17) results from an axial average [65]. Nevertheless, a weakly absorbing pump wavelength is chosen, with $\lambda = 1064$ nm, to mitigate such non-uniformity.

5.2.1. Polished Sample

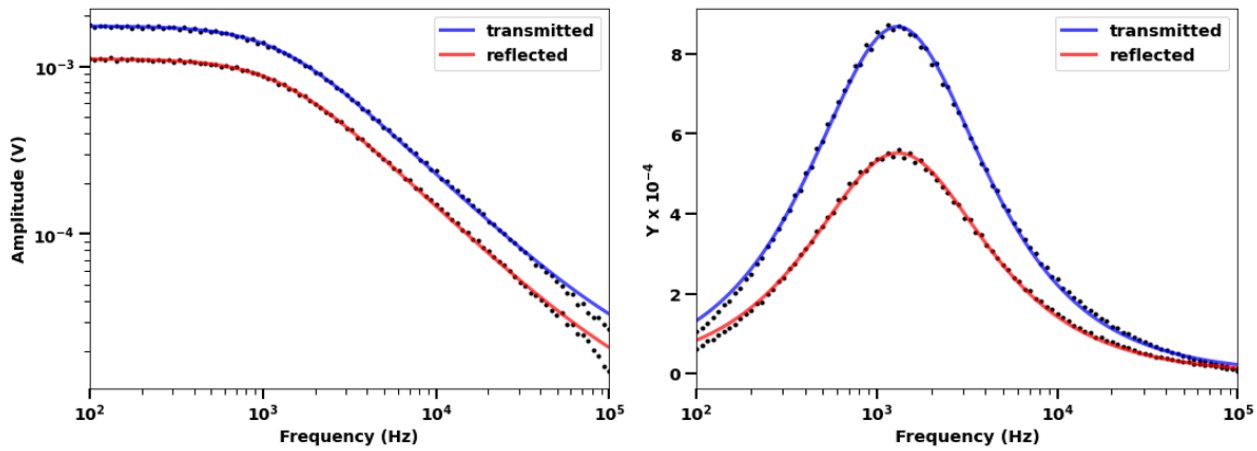

Figure 5.1. Real (left) and imaginary (right) parts of the AC MFCA signal of the transmitted and reflected probe beams versus modulation frequency for the Thick wafer. The symbols are the experimental data points, and the continuous lines are the best fit for the real and imaginary parts of Equation (2.17).

Figure 5.1 presents experimental results of the effective lifetime measurement of the Thick silicon wafer. The effective lifetimes extracted from fits of the real part of the AC MFCA signal are: (125.9 ± 0.7) μs for transmitted probe beam, and (124.6 ± 0.8) μs for reflected beam. The effective lifetimes extracted from fits of the imaginary part of the AC MFCA signal are: (122.1 ± 0.5) μs for transmitted probe beam, and (121.1 ± 0.5) μs for reflected beam. It can be seen that the Thick sample shows relatively high lifetimes, and the experimental results are very similar for different operational modes.

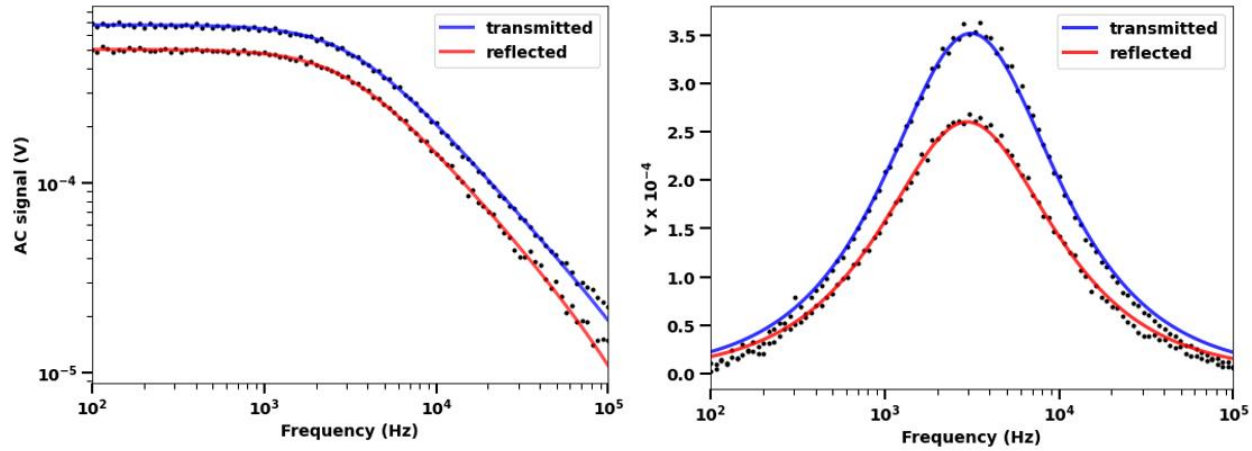

Figure 5.2. Real (left) and imaginary (right) parts of the AC MFCA signal of the transmitted and reflected probe beams versus modulation frequency for the Undoped sample. The symbols are the experimental data points, and the continuous lines are the best fit to the real and imaginary parts of Equation (2.17).

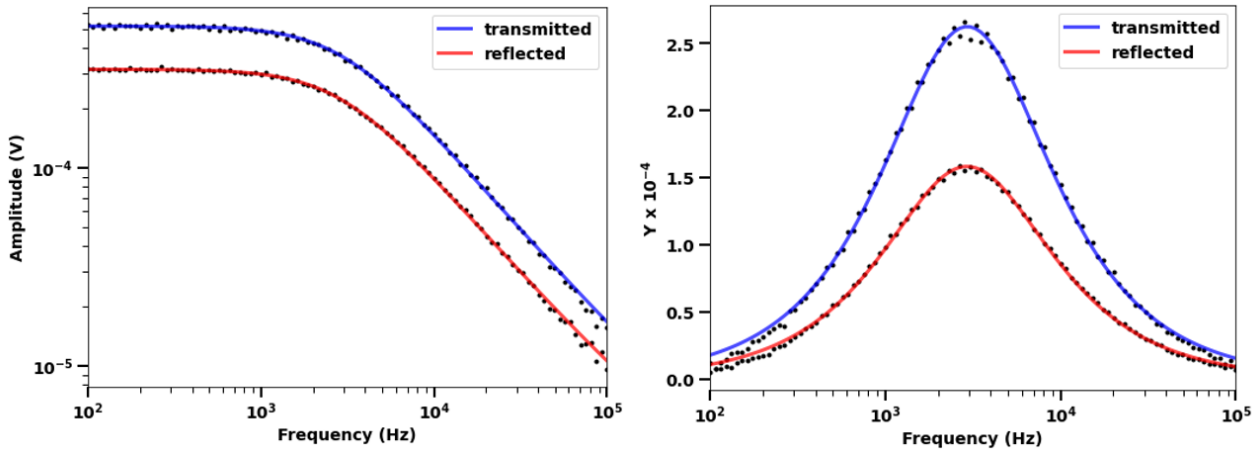

Figure 5.3. Real (left) and imaginary (right) parts of the AC MFCA signal of the transmitted and reflected probe beams versus modulation frequency for the El-Cat_2_9 sample. The symbols are the experimental data points, and the continuous lines are the best fit for the real and imaginary parts of Equation (2.17).

Figure 5.2 presents experimental results of the effective lifetime measurement of the Undoped silicon wafer. The effective lifetimes extracted from fits of the real part of the AC MFCA signal are: (50.4 ± 0.5) μs for transmitted probe beam, and (52.6 ± 0.5) μs for reflected beam. The effective lifetimes extracted from fits of the imaginary part of the AC MFCA signal are: (50.9 ± 0.4) μs for transmitted probe beam, and (53.6 ± 0.4) μs for reflected beam. The results from the transmitted mode and reflected experimental modes are also very similar.

Experimental results of the effective lifetime measurement of the El-Cat_2_9 silicon wafer are shown in Figure 5.3. The effective lifetimes extracted from fits of the real part of the AC MFCA signal are: (54.8 ± 0.5) μs for transmitted probe beam, and (55.4 ± 0.5) μs for reflected beam. The effective lifetimes extracted from fits of the imaginary part of the AC MFCA signal are: (54.2 ± 0.3) μs for transmitted probe beam, and (54.4 ± 0.3) μs for reflected beam. Both reflection and transmission mode techniques give similar values of the effective recombination lifetime of the El-Cat_2_9 sample.

Presented results allow me to make a conclusion that the measurement mode does not affect the

effective lifetime calculation. Even though for all examined samples the amplitude of the real signal in transmission mode is higher than the amplitude of the real reflected signal, the effective lifetime calculation depends only on the shape of the Lorentzian curve. A simple explanation of the difference in the amplitudes of reflected and transmitted signals is that in general more light is transmitted through the sample compared to the amount of light reflected from the back surface of the wafer. However, a more detailed analysis of multiple reflections of the probe beam inside the sample is given in the following section. This analysis gives a deeper explanation of the phenomenon seen in the experimental results.

5.2.2. Textured Sample

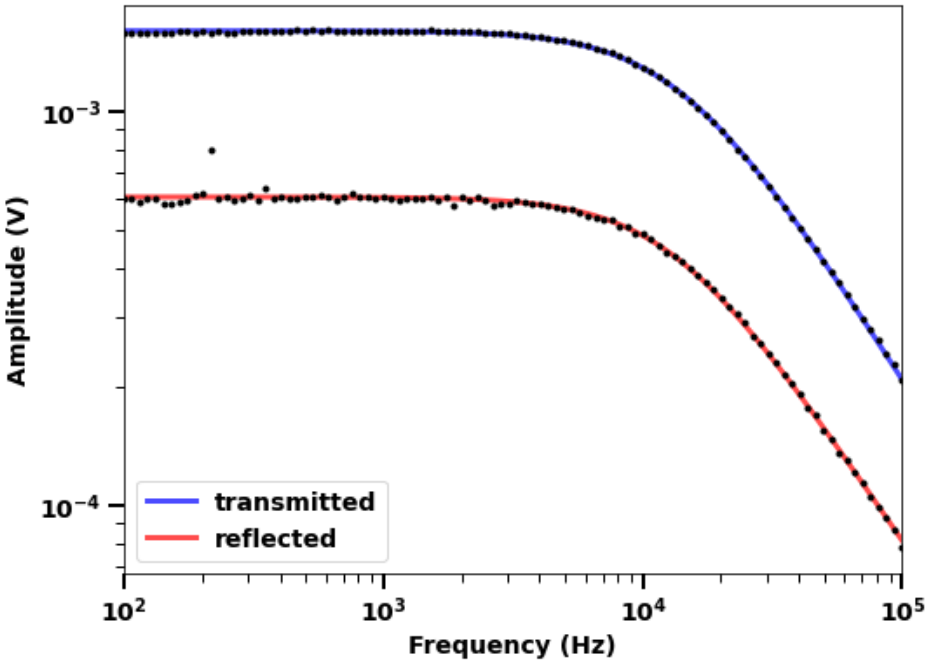

Figure 5.4. Real part of the raw AC MFCA signal of the transmitted and reflected prove beams versus modulation frequency for the El-Cat_15_2 textured sample. The symbols are the experimental data points, and the continuous lines are the best fit for the real and imaginary parts of Equation (2.17).

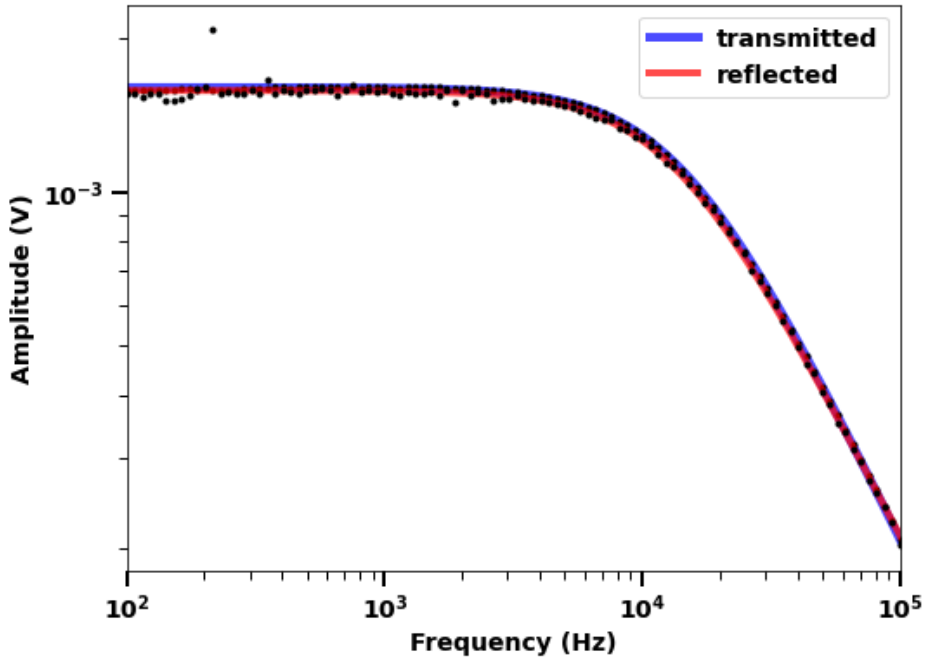

Figure 5.5. Real part of the calibrated AC MFCA signal of the transmitted and reflected probe beams versus modulation frequency for the El-Cat_15_2 textured sample. The symbols are the experimental data points, and the continuous lines are the best fit for the real and imaginary parts of Equation (2.17).

Figure 5.4 illustrates raw experimental results of the effective lifetime measurement of the El-Cat_15_2 textured sample. The effective lifetimes extracted from fits of the real part of the AC MFCA signal are: (11.7 ± 0.1) μs for transmitted probe beam, and (12.0 ± 0.4) μs for reflected beam. The amplitude of the reflected signal is significantly lower compared to the transmitted signal. This is due to the specifics of the experimental setup explained in 4.2. Assuming that the light reflected and transmitted from the surface of the textured sample has cosine distribution as in the case of the Lambertian surface, it is possible to calculate what would the amplitude of the reflected signal be if the system of lenses collected the same amount of light as the system collecting the transmitted part of the light. After completing this procedure, the amplitudes of the signals extracted from transmitted and reflected probe beams become nearly equal to each other as shown in Figure 5.5. This fact corresponds with the behavior of the Lambertian surface. Textured surfaces of the sample cause complete randomization of light propagation inside the medium. Therefore, half of the light that initially entered the wafer is escaped from the reflection side and the other half from the transmission side of the experimental setup. Exactly this behavior is seen in Figure 5.5, as the MFCA signal only represents the light that entered the wafer and was absorbed by free carriers. A more detailed analysis of the light entering the double-side textured sample and escaping from it will be given in the next section.

5.3. Analysis of Light Propagation

5.3.1. Double-side Polished Sample

When the light strikes a semiconductor interface, a fraction of the incident power is reflected while the rest is transmitted. In the case of a semiconductor with a weak absorption coefficient, the

entering light will undergo multiple internal reflections, partially transmitting out of the semiconductor each time it reaches an interface. The total light that emerges from the front surface is the reflected light and it is analyzed in the reflection geometry experiment, while the total light that emerges from the back surface is the transmitted light which is analyzed in the transmission geometry experiment. I have developed a model that determines the total power of the light emerging from the front and back surfaces of the sample. In the experiment, the small diameter of the probe beam with respect to the sample thickness in combination with the angle of incidence of the probe beam provide a relatively large separation of each subsequent internally reflected beam which leads to negligibly small overlap of these beams. Therefore, the derivation of the model includes only multiple reflections and excludes interference effects, which require significant and coherent beam overlap. The amplitudes of the modulated terms of the total reflected and transmitted powers are given by (see Appendix A):

$$P_{r,AC} = P_0 \frac{2R}{(1+R)^2} \eta W \sigma_{FCA} \, \Delta n_1 \tag{5.2}$$

$$P_{t,AC} = P_0 \frac{(1+R^2)}{(1+R)^2} \eta W \sigma_{FCA} \, \Delta n_1 \tag{5.3}$$

where P_0 is the incident power of the laser, R is the reflection coefficient of the sample, σ_{FCA} is the FCA cross-section, η is a factor describing the increase in pathlength through the wafer due to non-normal angle of propagation, and W is the wafer thickness. The amplitudes in (5.2) and (5.3) are measured in the experiment and determined from the low frequency response of the data presented in Figure 5.2. The ratio, $\mathcal{R}$, of the reflected and transmitted amplitudes of the modulated terms depends only on the reflectance properties of the sample. In the case of mixed polarization

of the incident light, the ratio is given by (see Appendix B):

$$\mathcal{R} = \frac{P_{r,AC}}{P_{t,AC}} = 2\sqrt{\frac{R_S^2(1+R_P)^4\, sin^2\,\theta + R_P^2(1+R_S)^4\, cos^2\,\theta}{(1+R_S^2)^2(1+R_P)^4 sin^2\theta + (1+R_P^2)^2(1+R_S)^4 cos^2\theta}} \qquad (5.4)$$

where R_S and R_P are the reflectance for the s and p polarized light respectively, and θ is the angle of polarization, with 0° being fully p-polarized and 90° being fully s-polarized. In the situation when there is only s-polarized ($R = R_S$) or p-polarized ($R = R_P$) light, Equation (5.4) reduces to a simple form:

$$\mathcal{R} = \frac{2R}{1+R^2} \qquad (5.5)$$

The derived ratio in Equation (5.4) explains the difference between the curves shown in Figure 5.1 - Figure 5.3. The amplitude of the transmitted signal will always be higher than the amplitude of the reflected signal. Experimentally, the ratio in Equation (5.4) can be determined directly by measuring the amplitudes of the modulated terms of the total transmitted (Equation (5.2)) and reflected (Equation (5.3)) powers of the probe beam and dividing (Equation (5.2)) by (Equation (5.3)). Using the angle of incidence and the known refractive index of the sample, we can calculate the reflectances R_S and R_P using the Fresnel equations to obtain values expected by theory. The results obtained for experimental and theoretical values of the ratio in Equation (5.5) for the Undoped silicon sample are presented in Figure 5.6.

In Figure 5.6, the experimental data points are in good agreement with the theoretical calculations for the full range of polarization angles. Changing the polarization of the probe beam from p to s

polarized allows us to vary the effective reflectance of the sample. Thus, the ratio from Equation (5.4) was examined for a range of different effective reflection coefficients while avoiding changes in the angle of incidence of the probe beam that could introduce undesired disturbance into the experimental procedure.

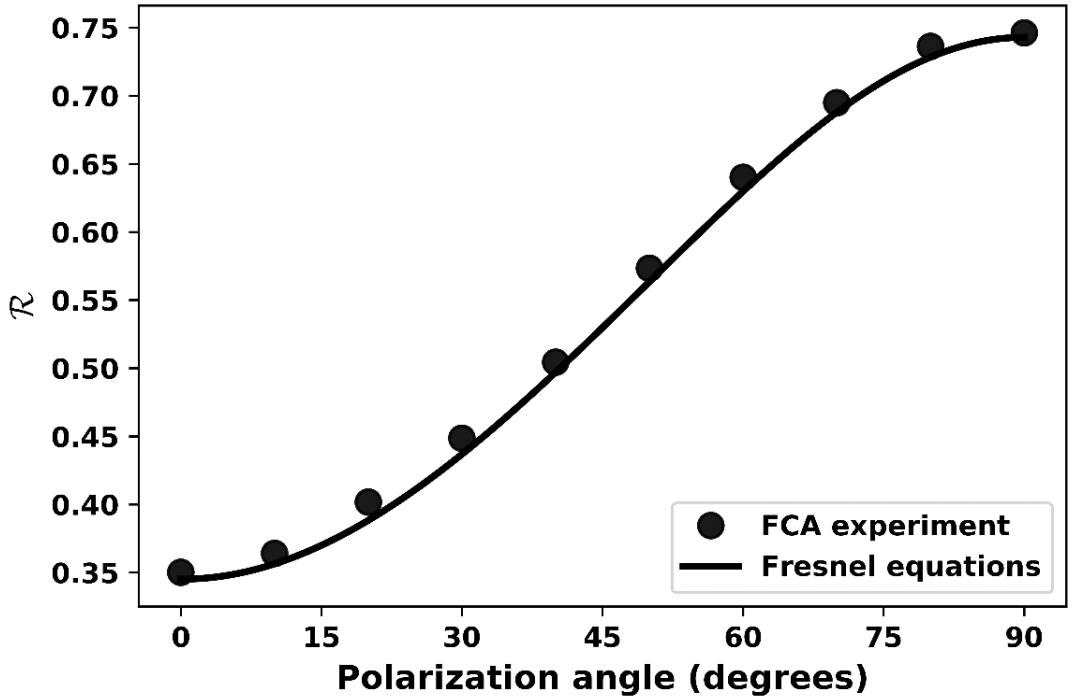

Figure 5.6. Ratio of the reflected and transmitted power of the probe beam versus the degree of polarization of the probe beam for the Undoped silicon sample.

A deeper analysis of Equation (5.4) provides information about the simple light trapping phenomenon which occurs within the double-side polished wafer. For the DC component of the incident probe beam, when R approaches 1, the transmission coefficient T approaches 0. However, in the same limit, the ratio from Equation (5.4) of the AC components of the reflected and transmitted beams approaches 1, meaning that their powers become equal, indicating that the light

inside the wafer loses information about the history of its path after multiple reflections. Indeed, when R approaches 1, most of the light is reflected from the surface but a small amount of light $(1-R)$ would still be able to enter the wafer. Because of the high reflection coefficient of the interfaces, the light that enters the wafer undergoes multiple reflections with high confinement. This situation is similar to the light trapping phenomenon in a double-side textured silicon wafer where total internal reflection confines to a high degree the light propagation randomized by the textured surfaces. Thus, the presented mathematical model can be expanded/transformed to the case of textured surfaces to analyze the light trapping efficiency of silicon wafers, which will be discussed in the next section.

It could also be useful to analyze the amplitude of the modulated part of the total absorbed power, which is equal to the sum of Equation (5.2) and Equation (5.3):

$$P_{a,AC} = \left[\frac{2R}{(1+R)^2} + \frac{(1+R^2)}{(1+R)^2}\right] P_0\, \eta W \sigma_{FCA}\, \Delta n_1 \tag{5.6}$$

which is simplified to:

$$P_{a,AC} = P_0\, \eta W \sigma_{FCA}\, \Delta n_1 \tag{5.7}$$

The amplitude of the modulated term of the total absorbed power is independent of the reflection coefficient of the silicon wafer.

5.3.2. Double-side Textured Sample

I have developed a model, similar to the one used for double-side polished samples, that determines the total power of the light emerging from the front and back surfaces of the textured sample. The model includes multiple reflections from the surface, where the light path of randomized rays is approximated by the average path of the rays scattered by the ideal Lambertian surface. The full derivation of the model is described in Appendix C. According to the model, the amplitudes of the modulated terms of the total reflected and transmitted powers are given by:

$$P_{t,AC} = P_0(1 - R_{tex})^2 \frac{f(1 + (1 - f')^2)}{(1 - (1 - f')^2)^2} \mathrm{W} Z \sigma_{FCA} \Delta n_1 \tag{5.8}$$

$$P_{r,AC} = P_0(1 - R_{tex})^2 \frac{2f(1 - f')}{(1 - (1 - f')^2)^2} \mathrm{W} Z \sigma_{FCA} \Delta n_1 \tag{5.9}$$

where P_0 is the incident power of the laser; σ_{FCA} is the FCA cross-section; f is the fraction of light escaping through the textured surface which is equal to $1/n^2$ and $f' = \mathrm{f}(1 - \mathrm{R_{tex}})$, where n is the refractive index of the sample; W is the wafer thickness; and Z is the average pathlength of randomized light rays in a single pass. The amplitudes of Equations (5.8) and (5.9) are measured experimentally and presented in Figure 5.5. Even though, in the experiment the reflected and transmitted diffuse probe beams are captured only partially by the sets of lenses, the symmetrical position of the lenses and an assumption that the textured surface is close to Lambertian allows to compare the amplitudes of acquired signals with each other. The ratio, $\mathcal{R}$, of the reflected and transmitted amplitudes of the modulated terms can be found by dividing Equation (5.9) by Equation (5.8):

$$\mathcal{R} = \frac{P_{r,AC}}{P_{t,AC}} = \frac{2(1-f)}{1+(1-f)^2} \tag{5.10}$$

For a silicon sample with refractive index $n = 3.48$ at 1550 nm, the ratio converges to 1. The ratio calculated from the experimental data is equal to 0.98 ± 0.02. This result shows that the derived model, even with considerable simplifications, is in good agreement with the experimental measurements, meaning that the properties of the surface of the textured sample are close to the properties of the Lambertian surface.

5.4. Additional Considerations

5.4.1. Interference effect

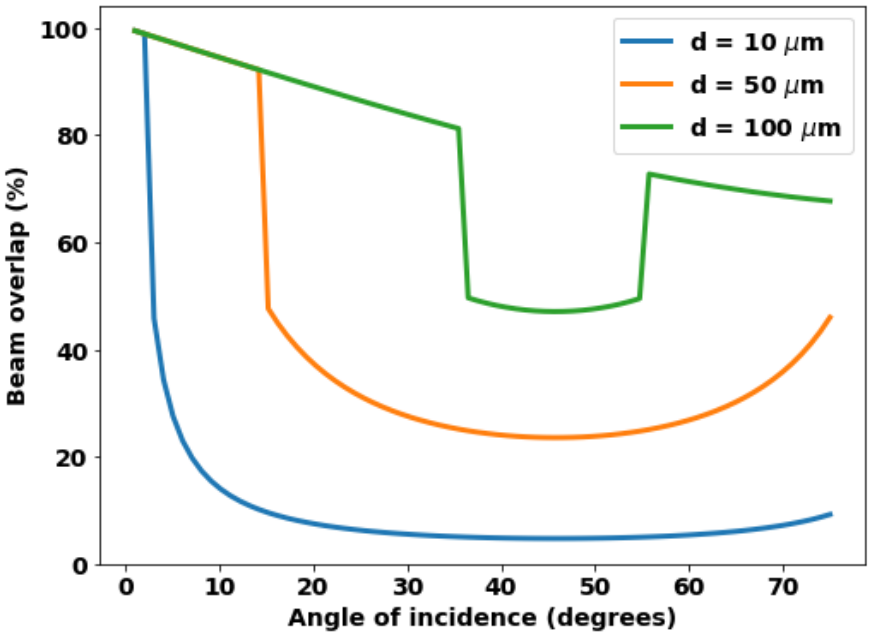

Figure 5.7. Overlap percentage of the light beam inside a 575 μm thick double-side polished silicon wafer versus incident angle of incoming beam for different diameters of the incident beam profile.

Multiple reflections of light inside a double-side polished silicon sample can lead to undesired interference effects which could negatively affect the results of effective lifetime measurements. Figure 5.7 shows the beam overlap percentage inside a 575 µm thick silicon sample for different incident angles of the beam and different diameters of the beam profile. The beam overlap percentage is calculated by analyzing the volume that the beam occupies during the initial pass and during the first reflection. The overlap percentage is then derived by calculating the ratio of the volumetric overlap of the abovementioned beam profiles to their total volume. An appropriate angle of incidence and beam diameter must be chosen to ensure a relatively small overlap of beams inside a sample. Appendix D provides a more detailed analysis of interference occurring in a double-side polished sample and shows, using FDTD simulation, that experimental conditions that ensure small beam overlap can help to avoid interference. Also, FDTD simulations show that surface roughness in the range of 200 nm or greater could lead to averaging of interference effect. Thus, the surfaces of the polished wafer must be smooth and perfectly parallel to each other to observe the interference effect.

5.4.2. Modulated Thermoreflectance

A modulated pump beam that hits a silicon sample causes modulation of the refractive index of the sample due to oscillating concentration of free carriers. This leads to modulation of reflectance (or modulated thermoreflectance) which can be present in the measured MFCA signal and negatively affect the effective lifetime measurements. Appendix A contains a detailed estimation of the change in refractive index relative to change in absorption coefficient. The ratio is equal to 0.012 for a 575 µm thick silicon sample. Therefore, the effects of free carrier photoreflectance can be safely neglected compared to free carrier photoabsorbance. However, for thin samples, thinner

than 21 μm, the opposite situation would occur and the thermoreflectance effects have to be considered.

5.5. Summary

In this chapter, I present a new approach for FCA measurement of silicon wafers in reflection mode that broadens a range of scenarios when the MFCA technique can be applied. In 5.2, I provide an experimental demonstration of the reflection mode MFCA technique applied to measure effective lifetimes of various polished and textured silicon samples. The results are compared with the transmission mode technique. In 5.3, I derive a theoretical model that describes the light propagation in polished and textured silicon samples and explains the difference in FCA signals acquired in reflection and transmission modes. In 5.4, I discuss some potential issues that may occur when using the MFCA technique and how to avoid them. Based on the results of this chapter, I have demonstrated a new experimental approach to conduct MFCA measurements that have not been published in scientific journals. This approach makes MFCA method more flexible in the choice of the geometry of the experimental setup and potentially more convenient to use an industrial production line.

6. Light Trapping Enhancement Calculation Using Free Carrier Absorption

6.1. Overview

In this chapter, I present a new experimental approach for measuring light trapping enhancement in a textured silicon wafer using the MFCA technique. It is known that the MFCA technique can provide information about various physical parameters of the polished silicon sample. In the previous chapter, it was shown that the MFCA technique can be used to measure the effective lifetime of a textured silicon sample, and a more detailed analysis of the MFCA signal can provide information about light propagation inside the sample. As the light stays longer in the textured silicon sample, more of it gets absorbed by free carriers, hence the FCA signal increases, and the enhancement of the light path compared to the sample thickness can be calculated. As a result, this technique can be applied to characterize the texturization quality of the surface comparing it to the Lambertian surface, and simultaneously measure the effective lifetime. A textured silicon wafer with thickness W can be represented by a sample with no light trapping but with the thickness of μW, where μ is the light path enhancement factor. Detailed theoretical derivation of this technique is given in the following section.

6.2. Theoretical Description of the Light Trapping Enhancement Measurement Technique

To derive the formula of the light path enhancement in a double side textured wafer, a normalized FCA signal acquired from a double-side polished silicon wafer must be analyzed first. From Appendix A, the DC and AC parts of the FCA signal received from the reflection mode measurements are given by:

$$P_{r,DC}^{DSP} = RP_0\left[1 + \frac{T^2}{1-R^2}\right] = P_0\frac{2R}{1+R} \tag{6.1}$$

$$P_{r,AC}^{DSP} = P_0\frac{2R}{(1+R)^2}\eta W\sigma_{FCA}\mathrm{m}\Delta n_0 \tag{6.2}$$

where m is the modulation depth defined as $\Delta n_1 = m\Delta n_0$. Thus, the normalized FCA signal from the reflection mode geometry is given by:

$$s_{DSP,r} \equiv \frac{P_{r,AC}^{DSP}}{P_{r,DC}^{DSP}} = \frac{\eta W\sigma_{FCA}m\Delta n_0}{1+R} \tag{6.3}$$

Using the same approach, the DC and AC parts of the FCA signal received from the transmission mode measurements of a double-side polished wafer are given by:

$$P_{t,DC}^{DSP} = \frac{P_0T^2}{1-R^2} = \frac{P_0(1-R)}{(1+R)} \tag{6.4}$$

$$P_{t,AC}^{DSP} = P_0 \frac{(1+R^2)}{(1+R)^2} \eta W \sigma_{FCA}\, m\Delta n_0 \tag{6.5}$$

And the normalized FCA signal from the transmission mode measurements is given by:

$$s_{DSP,t} \equiv \frac{P_{t,AC}^{DSP}}{P_{t,DC}^{DSP}} = \frac{(1+R^2)}{(1-R^2)} \eta W \sigma_{FCA} m\Delta n_0 \tag{6.6}$$

From Appendix C, the AC amplitudes of the FCA signal for a double-side textured silicon wafer for the transmission and reflection modes are equal and can be written as:

$$P_{t,AC} = P_{r,AC} = \frac{(1-R_{tex})^2}{f} P_0\, W \sigma_{FCA} m\Delta n_0 \tag{6.7}$$

The DC signals of the probe beam transmitted and reflected from a double-side textured silicon wafer are also equal:

$$P_{t,DC} = \frac{(1-R_{tex})^2}{2} P_0 \tag{6.8}$$

This leads to the normalized FCA signal for a double-side textured wafer:

$$\mathrm{s_{tex}} \equiv \frac{P_{t,AC}}{P_{t,DC}} = \frac{P_{r,AC}}{P_{r,\,DC}} = \; 2n^2 \mathrm{W} \sigma_{FCA}\, m\Delta n_0 \tag{6.9}$$

Equation (6.9) represents the ideal scenario where the surface of a textured silicon wafer is the perfect Lambertian surface, so the FCA signal of a textured sample is $2n^2$ higher compared to a

polished sample. This result is in ideal agreement with other theoretical models presented in the literature. In a real experiment, the normalized FCA signal for a textured sample can be written as:

$$s_{tex} = \mu \mathrm{W} \sigma_{FCA}\, m \Delta n_0 \tag{6.10}$$

where μ is the light path enhancement factor, which defines the quality of the texture and can be compared to the ideal Lambertian enhancement factor. μ can be understood as the absorption enhancement factor due to the increase of the average light path of the rays traveling inside a textured wafer.

In the quasi-steady state limit Δn_0, as shown in Equation (2.18), is equal to $G\tau$. The effective lifetime is known from fitting the Lorentzian curve, and the generation rate G is given by:

$$G = \frac{2 f_a P_{0,pu} \lambda_{pu}}{W A_p hc} \tag{6.11}$$

where $P_{0,pu}$ and λ_{pu} are the incident power and wavelength of the pump beam, respectively. A_p is the area of the incident pump beam. WA_p represents the volume the carriers occupy inside the sample. The diffusion factor is intentionally not included in the equation as the radius of the beam in the experiment is much larger than the diffusion length. However, for a double-side textured sample, randomized diffusion of light rays inside the sample must be considered to properly estimate the volume that free-carriers occupy. f_a is the fraction of pump power absorbed in the wafer, which can be measured directly in the experiment or calculated theoretically.

Substituting Equation (6.11) into $\Delta n_0 = G\tau$, the mean excess carrier density is given by:

$$\Delta n_0 = \frac{2 f_a P_{0,pu} \lambda_{pu}}{W A_p hc} \tau \tag{6.12}$$

Substituting this equation into Equation (*6.10*), the relationship between the reduced signal and the recombination lifetime is derived:

$$s_{tex} = \frac{2 m f_a P_{0,pu} \lambda_{pu}}{A_p hc} \mu \sigma_{FCA} \tau \tag{6.13}$$

Similarly, the relationship between the reduced signal and the recombination lifetime can be derived for a double-side polished sample. The relationship for a transmission mode signal is given by:

$$s_{DSP,t} = \frac{(1 + R^2)}{(1 - R^2)} \frac{2 m f_a P_{0,pu} \lambda_{pu}}{A_p hc} \eta \sigma_{FCA} \tau \tag{6.14}$$

The ratio between the reduced signal of the textured sample and the polished sample is described by:

$$\frac{s_{tex}}{s_{DSP,t}} = \frac{\mu}{\eta} \frac{\tau_{tex}}{\tau_{DSP}} \frac{f_{tex}}{f_{DSP}} \frac{A_{DSP}}{A_{tex}} \frac{(1 - R_{DSP}^2)}{(1 + R_{DSP}^2)} \tag{6.15}$$

Here all values with the *tex* subscript are related to the textured sample, and values with the *DSP* subscript are related to the polished sample. Equation (6.15) is valid for the case when the incident power of the pump beam is the same for both textured and polished samples. By rearranging Equation (6.15) we can derive a formula that determines the light trapping enhancement factor:

$$\frac{\mu}{\eta} = \frac{s_{tex}}{\tau_{tex}} \frac{\tau_{DSP}}{s_{DSP,t}} \frac{f_{DSP}}{f_{tex}} \frac{A_{tex}}{A_{DSP}} \frac{(1 + R_{DSP}^2)}{(1 - R_{DSP}^2)} \tag{6.16}$$

The right part of Equation (6.16), $\frac{f_{DSP}}{f_{tex}} \frac{A_{tex}}{A_{DSP}} \frac{(1+R_{DSP}^2)}{(1-R_{DSP}^2)}$, represents a constant value defined by the experimental setup. The left part, $\frac{s_{tex}}{\tau_{tex}} \frac{\tau_{DSP}}{s_{DSP,t}}$, is measured experimentally separately for polished and textured samples and gives a constant value. Multiplication of the two constant values gives the ratio $\frac{\mu}{\eta}$, where η is close to 1. Thus, the light trapping enhancement factor μ can be found.

6.3. Experimental Validation

6.3.1. Measurements with a Polished Sample

Two sets of measurements should be conducted to calculate the light trapping enhancement factor. Firstly, $\frac{s_{DSP,t}}{\tau_{DSP}}$ should be measured for a double-side polished sample, and then $\frac{s_{tex}}{\tau_{tex}}$ should be measured for a double-side textured sample. The incident power of the pump laser must be equal for both sets of measurements. In this work, the incident pump power is different, therefore Equation (6.16) must be rewritten in a different form:

$$\frac{\mu}{\eta} = \frac{s_{tex}}{\tau_{tex} P_{0,tex}} \frac{\tau_{DSP} P_{0,DSP}}{s_{DSP,t}} \frac{f_{DSP}}{f_{tex}} \frac{A_{tex}}{A_{DSP}} \frac{(1 + R_{DSP}^2)}{(1 - R_{DSP}^2)} \tag{6.17}$$

where $P_{0,tex}$ and $P_{0,DSP}$ are the incident pump powers used in experiments with textured and polished samples, respectively.

In this section, I present the experimental results of measuring the ratio $C_{DSP} = \frac{s_{DSP,t}}{\tau_{DSP} P_{0,DSP}} \frac{(1-R_{DSP}^2)}{(1+R_{DSP}^2)}$.

In the experiment, $s_{DSP,t}$ and τ_{DSP} are measured in transmission mode geometry for a range of incident pump powers changing from 100 mW to 600 mW. $s_{DSP,t}$ is calculated by measuring the AC and DC parts of the transmitted probe beam. R can be measured experimentally or calculated theoretically. Both theoretical and experimental values of R are equal to 0.18.

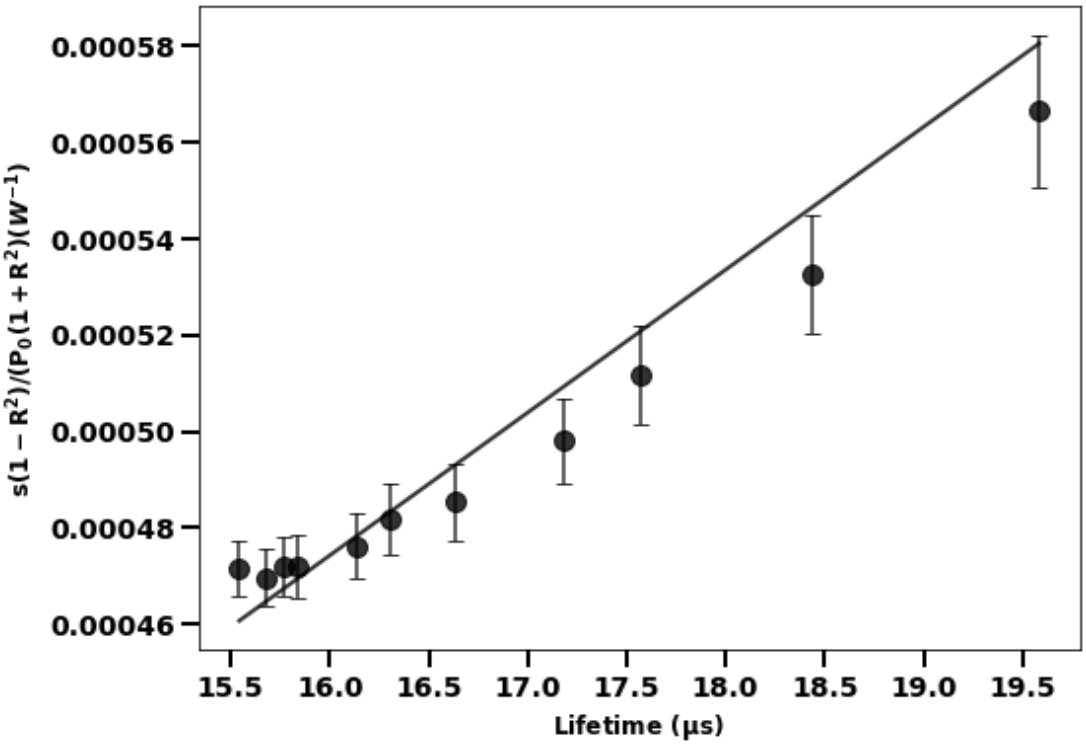

Figure 6.1. Normalized FCA signal of the EI-Cat_15_1 sample versus the effective lifetime. Measurements are done in the transmission mode geometry. The straight line is the best-fit line through zero. The highest injected carrier density in the EI-Cat_15_1 is 2.3 x 10^{15} cm^{-3}.

The slope of the best-fit line in Figure 6.1 is equal to $C_{DSP} = (2.96 \pm 0.01)\,\mathrm{x}\,10^{-5}\ \mathrm{W}^{-1}$. This value is used later to calculate μ.

6.3.2. Generation Rate in a Double-side Textured Sample

Before proceeding to the measurement of light path enhancement, the generation rate must be properly calculated for a double-side textured sample. Due to diffused spread of the light inside the textured sample free-carriers are created in the larger volume compared to the cylindrical generation volume in the double-side polished sample. In order to determine the generation volume, axial and lateral distribution of generated free carriers must be considered. The axial distribution is assumed to be uniform. The lateral distribution is assumed to have a larger radius than the initial radius of the gaussian pump beam. I have conducted a Monte Carlo simulation of light propagation and absorption in the double-side textured silicon wafer with the Lambertian surfaces to determine the lateral distribution of free carriers. The simulation model assumed that the direction of light rays entered the wafer is completely randomized following cosine distribution. Randomization of the ray direction happens after each reflection. Those rays which angle of propagation fall into the escape cone (see Equation (2.21)) escape from the medium with 100% transmission. The probability for the ray to be absorbed is calculated using Equation (2.19). The wafer is divided into equal layers along the axial direction and the probability of being absorbed is calculated upon entering each layer. The simulation model traces one million rays and calculates coordinates of the points where the rays get absorbed or escape from the medium. The initial distribution of rays incident to the sample surface follows a gaussian distribution resembling the gaussian pump beam. The radius of the incident laser beam is equal to 1.5 mm and the sample thickness is 325 μm.

Figure 6.2 shows the 2-dimensional distribution of point coordinates where the photons were absorbed and where some of them escaped from the medium. Fitting this distribution with a gaussian function I can find the radius of the pump beam spread inside the medium. Conducting the simulation several times and averaging the results, I found that the radius is equal to $w = (1.68 \pm 0.05)$ mm. Using this radius, a new cylindrical volume of carrier occupation can be calculated: $A_{tex} = \pi w^2$. Thus, the ratio of $\frac{A_{tex}}{A_{DSP}}$ is equal to 1.2.

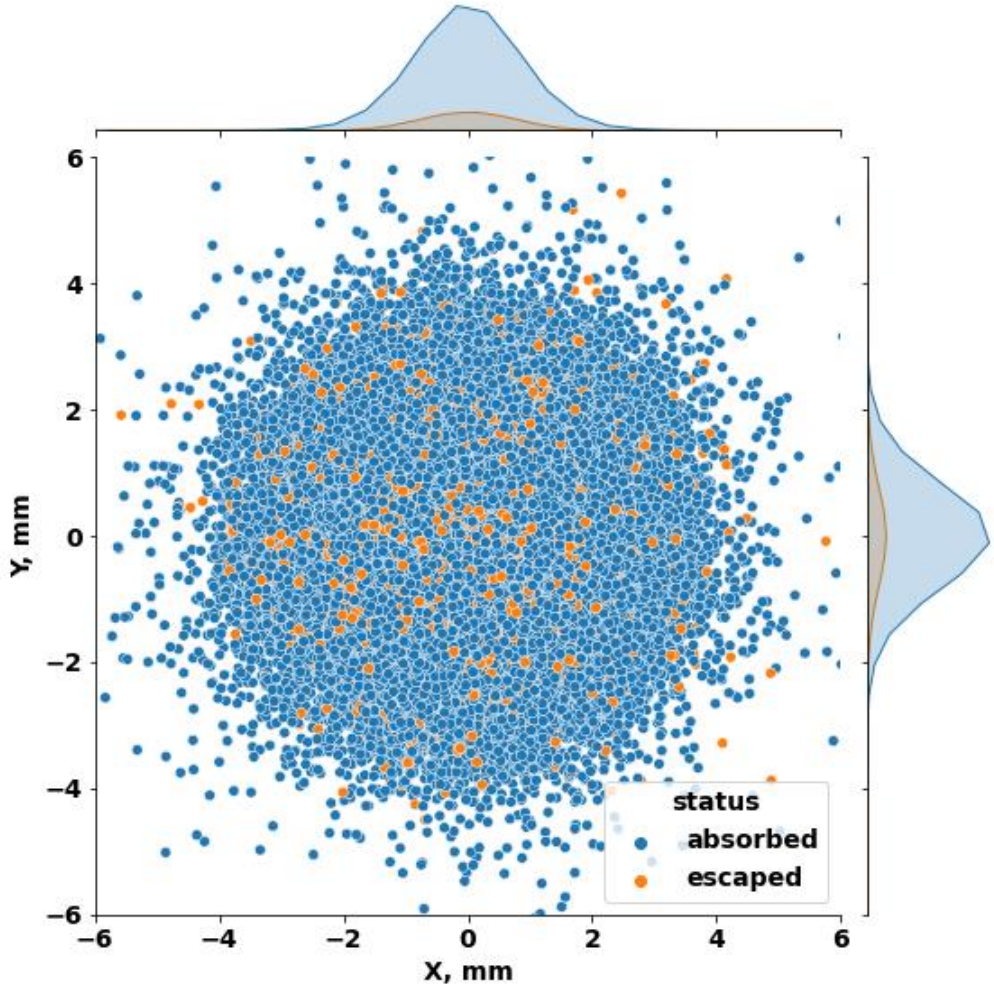

Figure 6.2. Distribution of absorbed and escaped photons in the double-side textured silicon sample.

6.3.3. Light Path Enhancement Measurement

The final step in the light path enhancement calculation is to find the ratio $C_{tex} = \frac{s_{tex}}{\tau_{tex} P_{0,tex}}$ for a double-side textured sample. s_{tex} is measured experimentally by collecting the AC and DC parts of the diffused transmitted probe beam. The measurements are done for a range of incident pump powers, $P_{0,tex}$, varying from 70 mW to 400 mW. The incident angle of the probe beam is equal to 30°.

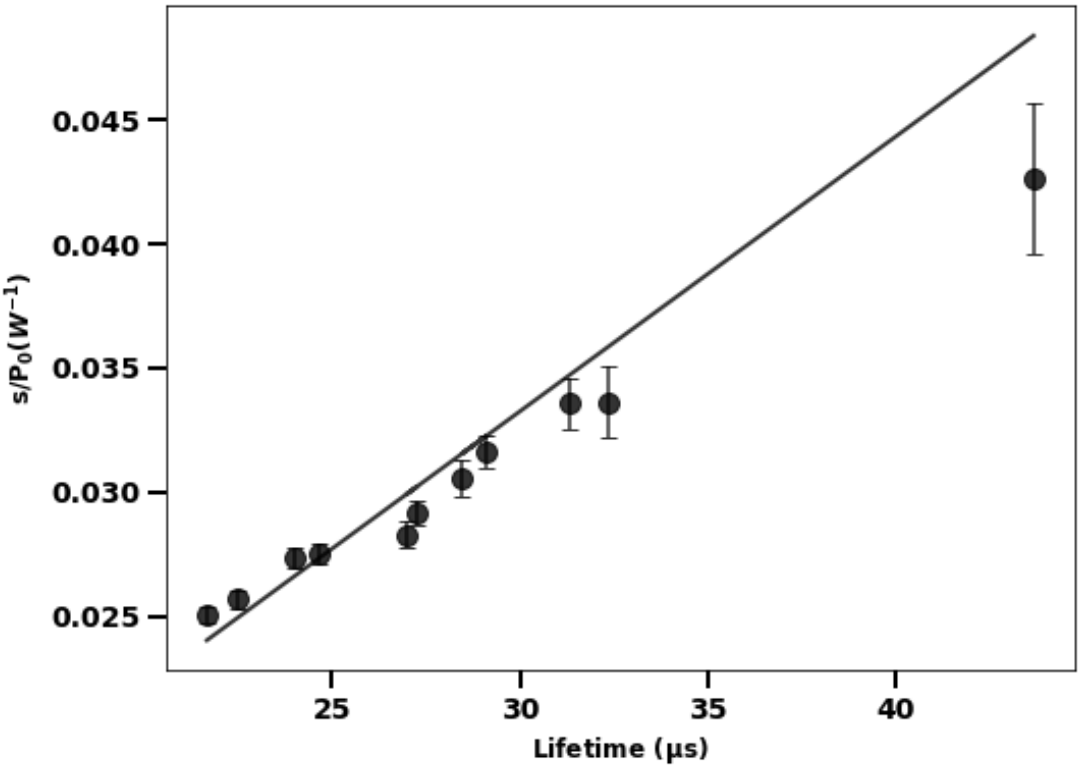

Figure 6.3. Normalized FCA signal of the El-Cat_15_2 sample versus the effective lifetime. Measurements are done in the transmission mode geometry. The straight line is the best-fit line through zero. The highest injected carrier density in the El-Cat_15_2 is 7.0 x 10^{15} cm^{-3}.

Figure 6.3 shows the results of the experiment. The slope of the best-fit line is equal to $C_{tex} = (1.11 \pm 0.01)$ x 10^{-3} W^{-1}. Now, as both C_{DSP} and C_{tex} are determined, Equation (6.17) can be written in a simpler form:

$$\frac{\mu}{\eta} = \frac{C_{text}}{C_{DSP}} \frac{f_{DSP}}{f_{tex}} \frac{A_{tex}}{A_{DSP}} \tag{6.18}$$

Here only the ratio of the absorption coefficients of the pump beam for the polished and textured samples, $\frac{f_{DSP}}{f_{tex}}$, is left unknown. Absorption coefficients f_{DSP} and f_{tex} can be measured experimentally or calculated theoretically. The absorption coefficient of the textured sample is calculated using Equation (C.34): $f_{tex} = 0.9$. The experimentally measured absorption

coefficient of the textured sample is equal to 0.88. Knowing the powers of the total reflected and transmitted light for the polished sample described in Equations (A.7), (A.8) and assuming that the FCA is negligible for the pump beam, we can derive the total absorptance of the polished sample:

$$f_{DSP} = 1 - R - (1 + Re^{-\alpha W})\frac{(1-R)^2 e^{-\alpha W}}{1 - R^2 e^{-2\alpha W}} \tag{6.19}$$

Choosing $\alpha = 10cm^{-1}$ for the 1064 nm pump beam, the theoretically calculated f_{DSP} is equal to 0.25, while experimentally measured f_{DSP} is equal to 0.23. The absorptance in the textured sample is approximately 3.5 times higher than in the polished sample. This shows a light trapping effect for the pump beam.

Now, as all components of Equation (6.18) are determined, and η is assumed to be equal to 1.04, the light path enhancement factor is calculated and equals to $\mu = 12.3 \pm 1$. This means that the average light path of the probe beam after entering the textured sample is 12.3 times the thickness of the sample. I have conducted several more experiments changing the incident angle of the probe beam to examine if the textured surface has angular selectivity patterns, meaning that for some incident angles the light path enhancement can be considerably higher or lower. The results of these experiments are presented in Table 2.

Table 2. Light path enhancement measured for a range of incident angles of the probe beam with respect to normal.

Incident angle	0°	15°	30°	45°
$\mu \pm 1$	11.0	11.7	12.3	10.3

The angle sweep experiment shows that, in general, angular selectivity has not been detected and the light path enhancement is close to 12 for all angles.

As shown in 6.2, the maximum light path enhancement factor for a double-side polished silicon wafer with the Lambertian surfaces is equal to 25. It is more than 2 times higher than the number measured in this work. This could mean that the texturization quality of the examined sample is relatively far from the Lambertian surface. In this case, the light inside the sample is not fully randomized and a considerable amount of light escapes from the sample during the first several passes leading to a reduction of the average light path. In addition, a lower rate of randomization causes angular selective transmission and reflection patterns. The SEM images of the examined sample also show that some of the surface pyramids are smaller than 1 μm in size, which leads to worse light trapping properties. However, the experimental results presented in 5.2.2 and the theoretical analysis of propagated light derived in 5.3.2 show that the reflected and transmitted light observed with the textured sample follow the Lambertian model. The results presented in Table 2 also do not show strong signs of angular selectivity. Finally, the experimentally measured absorption coefficient of the textured sample is in good agreement with the absorption coefficient calculated using the ray tracing simulation, and the theoretical model. Therefore, I assume that the quality of the textured surface examined in this experiment is close to Lambertian and I expect that μ must be higher than the experimental results. At the same time, there are no publications that could show high experimental values of light trapping enhancement in comparison with the Lambertian limit. Analysis of the light trapping efficiency of various silicon structures presented in [61] shows that experimentally measured values are in general significantly lower compared to values calculated numerically. This fact could be a sign that more theoretical studies are needed to investigate potential parasitic effects that could reduce the light trapping enhancement in real

structures. For example, parasitic band to band absorption is completely neglected in this study due to the extremely low absorption coefficient for a 1550 nm wavelength. The absorption coefficient of the overall parasitic absorption must be around 1.1 cm^{-1} to reduce the light path enhancement to 12.

Even though several experiments have been performed with different incident angles of the probe beam, angular selectivity of transmitted and reflected light could still be a reason of relatively low light path enhancement measured in the experiment. The surface of the examined sample consists of random pyramids with sizes ranging from 1 μm to 5 μm. According to the ray tracing simulations presented in the literature [34], propagation directions of light rays inside a textured silicon wafer become fully randomized only after several reflections. This means that a considerable fraction of light rays may be reflected/ transmitted non-diffusely and may transmit power in particular directions. These rays might not be collected by the system of lenses. At the same time, when they get collected and detected, they are mixed with the diffusely scattered light and the final signal is produced by the average of the two types of collected photons. As a result, total attenuation of the probe beam is decreased which leads to a lower value of the average light path of the probe beam inside a sample. Angular selective reflectance measurements must be performed to analyze this phenomenon more accurately.

The experimental procedure described in this chapter is only valid for the case when the reflected and transmitted radiation is close to Lambertian distribution. This ensures correct estimation of the amount of light collected with a system of lenses. In order to broaden this technique to samples with worse texturization quality, an integrating sphere must be used to collect all of the reflected or transmitted light.

6.3.4. Alternative approach

In this section, I present a slightly different approach to the light trapping enhancement factor calculation. It is based on Equation (6.13) that can be rewritten in a more convenient form:

$$s_{tex} = K\mu\sigma_{FCA}\tau \tag{6.20}$$

where K is given by:

$$K = \frac{2mf_aP_{0,pu}\lambda_{pu}}{A_phc} \tag{6.21}$$

Factor K consists of parameters that are defined by the experimental setup, while s_{tex} and τ are measured experimentally. Thus, the light path enhancement factor can be derived as:

$$\mu = \frac{s_{tex}}{K\sigma_{FCA}\tau} \tag{6.22}$$

The only unknown parameter left is σ_{FCA} – the FCA cross section. σ_{FCA} is a material constant that can be found in literature or experimentally. Experimental determination of σ_{FCA} is preferable as it can vary for different silicon samples. The most accurate approach is to measure σ_{FCA} of a polished silicon wafer before texturization procedure, or to measure σ_{FCA} of a polished silicon sample taken from the same wafer as the examined textured sample. A description of the σ_{FCA} measurement procedure is described in [14], [26]. In this work, σ_{FCA} is measured experimentally and equals to (4.8 ± 0.2) x $10^{-10}\mu m^2$.

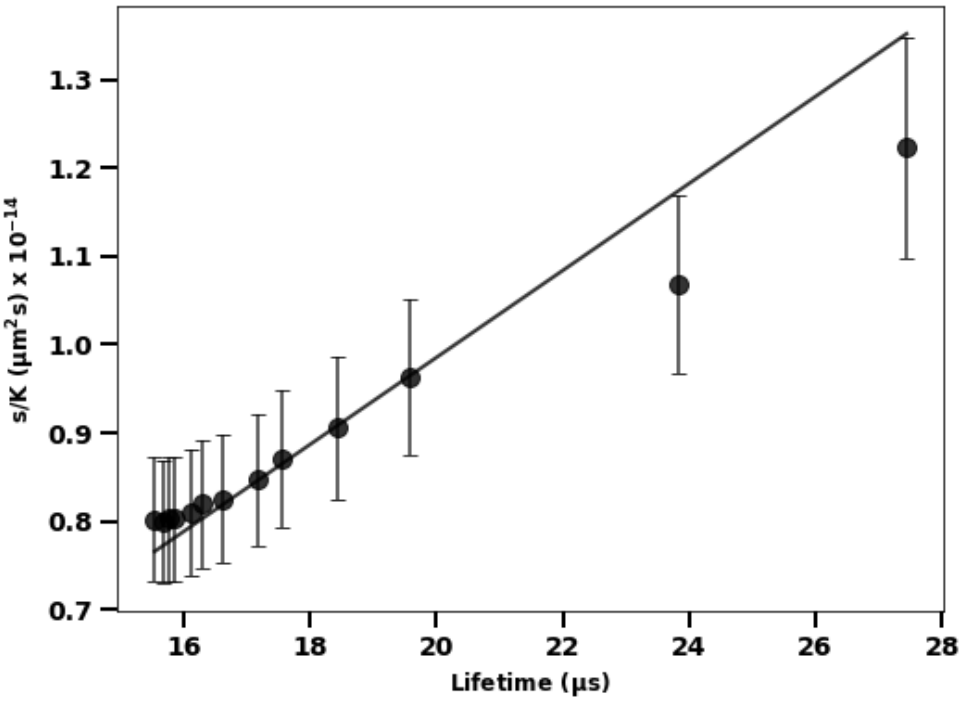

Figure 6.4. Plot of the normalized reduced signal versus effective lifetime for El-Cat_15_1 double-side polished sample. The straight line is the best-fit line through zero. The highest injected carrier density in the El-Cat_15_1 is 2.3 x 10^{15} cm^{-3}.

The normalized signal s/K is plotted as a function of the effective lifetime τ in Figure 6.4. The slope of the best-fit line divided by σ_{FCA} is the light path enhancement, which is equal to $\mu = 12 \pm 1$. Thus, if σ_{FCA} is known, there is no need to conduct measurements with a polished sample and the light path enhancement factor can be determined by conducting measurements only with a textured sample.

6.4. Summary

In this chapter, I present a new technique for measurement of light path enhancement in a textured silicon wafer. In 6.2, I provide a theoretical description of the technique. In 6.3, I present experimental results and explain the details that must be considered in the experimental procedure. The obtained results are analyzed and compared to the theoretical limit. Based on the results of

this chapter, I have demonstrated for the first time the pump/probe MFCA technique that can be used to analyze the quality of the textured surface by measuring the light path enhancement factor. This method significantly broadens the application of the pump/probe MFCA technique as it can be used to measure the effective lifetime and to control the texturization quality of silicon surface simultaneously.

7. Conclusion and Future Work

7.1. Conclusion

In this dissertation, I have demonstrated a new experimental approach that can be used in MFCA measurements to determine the effective lifetime of silicon wafers. I have shown how MFCA measurements can be done in the reflection mode geometry and compared it to the conventional approach – transmission mode geometry. It has been shown that the results of lifetime measurements are identical for the reflection mode technique and the conventional transmission mode technique. The experimental procedure has been presented to measure the effective lifetime of textured samples. A comprehensive analysis of light propagation in a double-side polished and double-side textured silicon samples has been derived. The analysis is validated with experimental results. The derived theoretical model of light propagation has revealed potential light trapping capabilities in a double-side polished silicon sample, as well as examined the reflection and transmission properties of a double-side textured sample. It has been shown that the reflection mode MFCA technique can be a new additional option for noncontact characterization of silicon wafers and can make the MFCA method more flexible in the choice of the geometry of the experimental setup.

I have also developed a new experimental technique that uses the MFCA method to measure the light trapping enhancement in a textured silicon wafer. This technique can be used to simultaneously analyze the quality of the surface texture and measure the effective lifetime of a silicon wafer or a solar cell. The model explaining propagation of light inside a textured silicon wafer has been derived and the experimental procedure has been fully described. The technique has shown reasonable experimental results, which, however, considerably deviate from the

theoretical limit. Most likely, the reason for the deviation is the low surface quality of the examined wafer compared to the Lambertian surface. It is nearly impossible to calculate the light path enhancement factor in the given sample theoretically, therefore the experimental results can only be compared with the Lambertian limit. However, some undetermined physical processes could be a reason for the low light path enhancement factor measured in the experiment, as there is no evidence of a high light trapping enhancement factor measured experimentally in literature.

To sum up, the experimental techniques demonstrated in this dissertation considerably broaden the application of the MFCA method. The reflection mode MFCA technique provides higher flexibility in the choice of the geometry of the experimental setup. The light path enhancement measurement technique based on the MFCA method provides an opportunity to use a single technique and experimental apparatus to measure two crucial characteristics of silicon solar cells.

7.2. Future Work

The experimental results of the light path enhancement factor measured in this work should be compared to the experimental results that can be received using other techniques. This should be done to understand whether the developed technique provides correct results. Also, an experimental setup with an integrating sphere should be used to collect all reflected and transmitted radiation. This can increase the accuracy of measurements, especially for wafers with relatively low surface quality. Performing measurements for different types of surface textures (random pyramids of different sizes, inverted pyramids), light trapping schemes (with/without back reflector, one-side polished and one-side textured), and for wavelengths of the probe beam can help to check the accuracy of the derived model explaining the light propagation inside a textured

silicon wafer. It also would be great to test the demonstrated technique with plasmonic light trapping structures on silicon.

References

[1] A. Blakers, N. Zin, K. R. McIntosh, and K. Fong, "High Efficiency Silicon Solar Cells," *Energy Procedia*, vol. 33, pp. 1–10, 2013.

[2] F. Shimura, T. Okui, and T. Kusama, "Noncontact minority-carrier lifetime measurement at elevated temperatures for metal-doped Czochralski silicon crystals," *J. Appl. Phys.*, vol. 67, no. 11, pp. 7168–7171, 1990.

[3] V. Petrova-koch, *High-Efficient Low-Cost Photovoltaics*, vol. 140. Berlin, Heidelberg: Springer Berlin Heidelberg, 2009.

[4] S. Rein, *Lifetime Spectroscopy*, vol. 85. Berlin, Heidelberg: Springer Berlin Heidelberg, 2005.

[5] J. Linnros, "Carrier lifetime measurements using free carrier absorption transients. I. Principle and injection dependence," *J. Appl. Phys.*, vol. 84, no. 1, pp. 275–283, Jul. 1998.

[6] S. W. Glunz, A. B. Sproul, W. Warta, and W. Wettling, "Injection-level-dependent recombination velocities at the Si-SiO 2 interface for various dopant concentrations," *J. Appl. Phys.*, vol. 75, no. 3, pp. 1611–1615, 1994.

[7] M. P. Halsall, I. F. Crowe, J. Mullins, R. A. Oliver, M. J. Kappers, and C. J. Humphreys, "Photomodulated Reflectivity Measurement of Free-Carrier Dynamics in InGaN/GaN Quantum Wells," *ACS Photonics*, vol. 5, no. 11, pp. 4437–4446, 2018.

[8] R. Yano, Y. Hirayama, S. Miyashita, H. Sasabu, N. Uesugi, and S. Uehara, "Pump-probe spectroscopy of low-temperature grown gaAs for carrier lifetime estimation: Arsenic pressure dependence of carrier lifetime during MBE crystal growth," *Phys. Lett. Sect. A Gen. At. Solid State Phys.*, vol. 289, no. 1–2, pp. 93–98, 2001.

[9] A. Mohanta, D. J. Jang, M. S. Wang, and L. W. Tu, "Time-integrated photoluminescence and pump-probe reflection spectroscopy of Si doped InN thin films," *J. Appl. Phys.*, vol. 115, no. 4, 2014.

[10] A. Mandelis and R. E. Wagner, "Quantitative deconvolution of photomodulated thermoreflectance signals from Si and Ge semiconducting samples," *Japanese J. Appl. Physics, Part 1 Regul. Pap. Short Notes Rev. Pap.*, vol. 35, no. 3, pp. 1786–1797, 1996.

[11] A. Mandelis, J. Batista, and D. Shaughnessy, "Infrared photocarrier radiometry of semiconductors: Physical principles, quantitative depth profilometry, and scanning imaging of deep subsurface electronic defects," *Phys. Rev. B - Condens. Matter Mater. Phys.*, vol. 67, no. 20, pp. 1–18, 2003.

[12] M. K. Basher, M. K. Hossain, M. J. Uddin, M. A. R. Akand, and K. M. Shorowordi, "Effect of pyramidal texturization on the optical surface reflectance of monocrystalline photovoltaic silicon wafers," *Optik (Stuttg).*, vol. 172, pp. 801–811, 2018.

[13] S. O. Kasap, *Optoelectronics and Photonics: Principles and Practices*. Prentice Hall, 2001.

[14] K. M. W. Boyd, "Free-Carrier Pump / Probe Spectroscopy," *McMaster Univ.*, 2018.

[15] D. B. M. Klaassen, "A unified mobility model for device simulation-I. Model equations and concentration dependence," *Solid State Electron.*, vol. 35, no. 7, pp. 953–959, 1992.

[16] D. K. Schroder, R. N. Thomas, and J. C. Swartz, "Free Carrier Absorption in Silicon," *IEEE J. Solid-State Circuits*, vol. 13, no. 1, pp. 180–187, Feb. 1978.

[17] P. Zheng, F. E. Rougieux, D. Macdonald, and A. Cuevas, "Parameterization of carrier mobility sum in silicon as a function of doping, temperature and injection level: Extension to p-type silicon," *2014 IEEE 40th Photovolt. Spec. Conf. PVSC 2014*, pp. 129–134, 2014.

[18] S. C. Baker-Finch, K. R. McIntosh, D. Yan, K. C. Fong, and T. C. Kho, "Near-infrared free carrier absorption in heavily doped silicon," *J. Appl. Phys.*, vol. 116, no. 6, 2014.

[19] B. K. Ridley, *Quantum Processes in Semiconductors*, vol. 55, no. 4. Oxford University Press, 2013.

[20] J. Isenberg and W. Warta, "Free carrier absorption in heavily doped silicon layers," *Appl. Phys. Lett.*, vol. 84, no. 13, pp. 2265–2267, 2004.

[21] G. N. Koskowich, M. Soma, and R. B. Darling, "Near-infrared free-carrier optical absorption in silicon: Effect of first-order phonon-assisted scattering in a nonparabolic conduction band," *Phys. Rev. B*, vol. 41, no. 5, pp. 2944–2947, 1990.

[22] J. Meitzner, F. G. Moore, B. M. Tillotson, S. D. Kevan, and G. L. Richmond, "Time-resolved measurement of free carrier absorption, diffusivity, and internal quantum efficiency in silicon," *Appl. Phys. Lett.*, vol. 103, no. 9, 2013.

[23] M. De Laurentis and A. Irace, "Optical Measurement Techniques of Recombination Lifetime Based on the Free Carriers Absorption Effect," *J. Solid State Phys.*, vol. 2014, no. Ilm, pp. 1–19, 2014.

[24] V. Grivickas and J. Linnros, "Carrier Lifetime: Free Carrier Absorption, Photoconductivity, and Photoluminescence," in *Characterization of Materials*, Hoboken, NJ, USA: John Wiley & Sons, Inc., 2012.

[25] M. Rosling, H. Bleichner, P. Jonsson, and E. Nordlander, "The ambipolar diffusion coefficient in silicon: Dependence on excess-carrier concentration and temperature," *J. Appl. Phys.*, vol. 76, no. 5, pp. 2855–2859, Sep. 1994.

[26] K. M. W. Boyd and R. N. Kleiman, "Quasi-Steady-State Free Carrier Absorption Measurements of Effective Carrier Lifetime in Silicon," *IEEE J. Photovoltaics*, vol. 9, no. 1, pp. 64–71, 2019.

[27] K. L. Luke and L. J. Cheng, "Analysis of the interaction of a laser pulse with a silicon wafer: Determination of bulk lifetime and surface recombination velocity," *J. Appl. Phys.*, vol. 61, no. 6, pp. 2282–2293, 1987.

[28] M. A. Green, "Lambertian light trapping in textured solar cells and light-emitting diodes: Analytical solutions," *Prog. Photovoltaics Res. Appl.*, vol. 10, no. 4, pp. 235–241, 2002.

[29] E. Yablonovitch, "Statistical Ray Optics.," *J. Opt. Soc. Am.*, vol. 72, no. 7, pp. 899–907,

1982.

[30] A. Goetzberger, “Optical Confinement in Thin Si-Solar Cells By Diffuse Back Reflectors.,” *Conference Record of the IEEE Photovoltaic Specialists Conference*. pp. 867–870, 1981.

[31] P. Campbell and M. A. Green, “Light trapping properties of pyramidally textured surfaces,” *J. Appl. Phys.*, vol. 62, no. 1, pp. 243–249, 1987.

[32] A. Luque and J. C. Miñano, “Optical aspects in photovoltaic energy conversion,” *Sol. Cells*, vol. 31, no. 3, pp. 237–258, 1991.

[33] U. Rau, U. W. Paetzold, and T. Kirchartz, “Thermodynamics of light management in photovoltaic devices,” *Phys. Rev. B - Condens. Matter Mater. Phys.*, vol. 90, no. 3, pp. 1–16, 2014.

[34] S. Manzoor, M. Filipič, A. Onno, M. Topič, and Z. C. Holman, “Visualizing light trapping within textured silicon solar cells,” *J. Appl. Phys.*, vol. 127, no. 6, 2020.

[35] Z. Yu, A. Raman, and S. Fan, “Fundamental limit of nanophotonic light trapping in solar cells,” *Proc. Natl. Acad. Sci. U. S. A.*, vol. 107, no. 41, pp. 17491–17496, 2010.

[36] I. Tobías, A. Luque, and A. Martí, “Light intensity enhancement by diffracting structures in solar cells,” *J. Appl. Phys.*, vol. 104, no. 3, 2008.

[37] V. E. Ferry, L. A. Sweatlock, D. Pacifici, and H. A. Atwater, “Plasmonic Nanostructure Design for Efficient Light Coupling into Solar Cells,” *Nano Lett.*, vol. 8, no. 12, pp. 4391–4397, Dec. 2008.

[38] P. N. Saeta, V. E. Ferry, D. Pacifici, J. N. Munday, and H. A. Atwater, “How much can guided modes enhance absorption in thin solar cells?,” *Opt. Express*, vol. 17, no. 23, p. 20975, 2009.

[39] S. B. Mallick, M. Agrawal, and P. Peumans, “Optimal light trapping in ultra-thin photonic crystal crystalline silicon solar cells,” *Opt. Express*, vol. 18, no. 6, p. 5691, 2010.

[40] D. Derkacs, S. H. Lim, P. Matheu, W. Mar, and E. T. Yu, “Improved performance of amorphous silicon solar cells via scattering from surface plasmon polaritons in nearby metallic nanoparticles,” *Appl. Phys. Lett.*, vol. 89, no. 9, pp. 1–4, 2006.

[41] D. M. Schaadt, B. Feng, and E. T. Yu, “Enhanced semiconductor optical absorption via surface plasmon excitation in metal nanoparticles,” *Appl. Phys. Lett.*, vol. 86, no. 6, pp. 1–3, 2005.

[42] C. Eminian, F.-J. Haug, O. Cubero, X. Niquille, and C. Ballif, “Photocurrent enhancement in thin film amorphous silicon solar cells with silver nanoparticles,” *Prog. Photovoltaics Res. Appl.*, vol. 19, no. 3, pp. 260–265, May 2011.

[43] V. E. Ferry, A. Polman, and H. A. Atwater, “Light trapping in plasmonic solar cells,” *Opt. InfoBase Conf. Pap.*, vol. 18, no. June, pp. 237–245, 2011.

[44] F. J. Beck and K. Catchpole, “Red-shifting the surface plasmon resonance of silver nanoparticles for light trapping in solar cells,” *Mater. Res. Soc. Symp. Proc.*, vol. 1101, pp. 44–53, 2008.

[45] M. Kunst and G. Beck, "The study of charge carrier kinetics in semiconductors by microwave conductivity measurements," *J. Appl. Phys.*, vol. 60, no. 10, pp. 3558–3566, Nov. 1986.

[46] M. Schöfthaler and R. Brendel, "Sensitivity and transient response of microwave reflection measurements," *J. Appl. Phys.*, vol. 77, no. 7, pp. 3162–3173, 1995.

[47] R. A. Sinton and A. Cuevas, "Contactless determination of current-voltage characteristics and minority-carrier lifetimes in semiconductors from quasi-steady-state photoconductance data," *Applied Physics Letters*, vol. 69, no. 17. pp. 2510–2512, 1996.

[48] J. S. Swirhun, R. A. Sinton, M. K. Forsyth, and T. Mankad, "Contactless measurement of minority carrier lifetime in silicon ingots and bricks," *Prog. Photovoltaics Res. Appl.*, vol. 19, no. 3, pp. 313–319, May 2011.

[49] J. A. Giesecke, B. Michl, F. Schindler, M. C. Schubert, and W. Warta, "Minority carrier lifetime of silicon solar cells from quasi-steady-state photoluminescence," *Sol. Energy Mater. Sol. Cells*, vol. 95, no. 7, pp. 1979–1982, 2011.

[50] J. A. Giesecke, M. C. Schubert, D. Walter, and W. Warta, "Minority carrier lifetime in silicon wafers from quasi-steady-state photoluminescence," *Appl. Phys. Lett.*, vol. 97, no. 9, 2010.

[51] T. Trupke and R. A. Bardos, "Photoluminescence: A surprisingly sensitive lifetime technique," *Conf. Rec. IEEE Photovolt. Spec. Conf.*, pp. 903–906, 2005.

[52] L. Huldt, "Optical Method for Determining Carrier Lifetimes in Semiconductors," *Phys. Rev. Lett.*, vol. 2, no. 1, pp. 3–5, Jan. 1959.

[53] N. G. Nilsson, "Determination of carrier lifetime, diffusion length, and surface recombination velocity in semiconductors from photo-excited infrared absorption," *Solid. State. Electron.*, vol. 7, no. 6, pp. 455–463, Jun. 1964.

[54] F. Sanii, R. J. Schwartz, R. F. Pierret, and W. M. Au, "The measurement of bulk and surface recombination by means of modulated free carrier absorption," in *Conference Record of the Twentieth IEEE Photovoltaic Specialists Conference*, 1988, vol. 4, pp. 575–580 vol.1.

[55] K. M. W. Boyd and R. N. Kleiman, "Single-beam lifetime measurements via self-induced optical absorption," *Opt. Express*, vol. 27, no. 4, p. 4445, 2019.

[56] J. Opsal, M. W. Taylor, W. L. Smith, and A. Rosencwaig, "Temporal behavior of modulated optical reflectance in silicon," *J. Appl. Phys.*, vol. 61, no. 1, pp. 240–248, 1987.

[57] K. Petursson, "Determining effective lifetime of minority carriers in silicon through modulated free carrier absorption," *McMaster Univ.*, 2017.

[58] E. Forniés, C. Zaldo, and J. M. Albella, "Control of random texture of monocrystalline silicon cells by angle-resolved optical reflectance," *Sol. Energy Mater. Sol. Cells*, vol. 87, no. 1–4, pp. 583–593, 2005.

[59] H. Mäckel, H. Holst, M. Löhmann, E. Wefringhaus, and P. P. Altermatt, "Detailed Analysis of Random Pyramid Surfaces with Ray Tracing and Image Processing," *IEEE J.*

Photovoltaics, vol. 6, no. 6, pp. 1456–1465, 2016.

[60] K. R. McIntosh and S. C. Baker-Finch, "A Parameterization of Light Trapping in Wafer-Based Solar Cells," *IEEE J. Photovoltaics*, vol. 5, no. 6, pp. 1563–1570, 2015.

[61] C. S. Schuster, A. Bozzola, L. C. Andreani, and T. F. Krauss, "How to assess light trapping structures versus a Lambertian Scatterer for solar cells?," *Opt. Express*, vol. 22, no. S2, p. A542, 2014.

[62] M. Ernst and R. Brendel, "Lambertian light trapping in thin crystalline macroporous Si layers," *Phys. Status Solidi - Rapid Res. Lett.*, vol. 8, no. 3, pp. 235–238, 2014.

[63] C. Barugkin, T. Allen, T. K. Chong, T. P. White, K. J. Weber, and K. R. Catchpole, "Light trapping efficiency comparison of Si solar cell textures using spectral photoluminescence," *Opt. Express*, vol. 23, no. 7, p. A391, 2015.

[64] M. Ledinský *et al.*, "Light trapping in thin-film solar cells measured by Raman spectroscopy," *Appl. Phys. Lett.*, vol. 105, no. 11, 2014.

[65] R. Soref and B. Bennett, "Electrooptical effects in silicon," *IEEE J. Quantum Electron.*, vol. 23, no. 1, pp. 123–129, Jan. 1987.

Appendix A Calculation of the Amplitudes of the Modulated Terms of the Total Reflected and Transmitted Powers for the Double-side Polished Sample

When light strikes a semiconductor interface, a fraction of the incident power is reflected while the rest is transmitted. If the absorption coefficient of the semiconductor is weak then the light that enters the semiconductor will undergo multiple reflections, partially transmitting out of the semiconductor each time it reaches an interface. The total light that emerges from the front surface is the reflected light, while the total light that emerges from the back surface is the transmitted light.

The reflectance and transmittance of a slab are given by considering an infinite number of bounces. Each light ray that traverses the wafer is attenuated by a factor $e^{-\eta\beta}$. Here β is an absorption factor which in general has contributions from band-to-band and free-carrier absorption. The factor $\eta = \sec\psi$ describes the increase in pathlength through the wafer due to a non-normal angle of propagation, where ψ is the angle of propagation from normal through the wafer.

For an incident power, P_0, the reflected power from the first surface is:

$$P_{r0} = RP_0, \tag{A.1}$$

where R is the interfacial reflection coefficient. The second reflected beam is given by:

$$P_{r1} = T^2 R e^{-2\eta\beta} P_0. \tag{A.2}$$

Here T is the interfacial transmission coefficient (where $R + T = 1$), which is squared because the initial light ray has to transmit into the wafer, then transmit out again. The factor of 2 in the attenuation factor accounts for two passes through the wafer. The next reflected beam is:

$$P_{r2} = T^2 R^3 e^{-4\eta\beta} P_0. \tag{A.3}$$

Generalizing to the m^{th} reflected ray:

$$P_{rm} = T^2 R^{2m-1} e^{-2m\eta\beta} P_0, \tag{A.4}$$

where $m = 1, 2, ...$

Similar calculations are performed for the transmitted power. The total reflection and transmission are then given by:

$$P_r = RP_0 + \frac{T^2}{R} P_0 \sum_{m=1}^{\infty} \left[R^2 e^{-2\eta\beta}\right]^m, \tag{A.5}$$

$$P_t = \frac{T^2}{R^2 e^{-\eta\beta}} P_0 \sum_{m=1}^{\infty} \left[R^2 e^{-2\eta\beta}\right]^m. \tag{A.6}$$

Performing the sums, the total reflection and transmission become:

$$P_r = RP_0\left[1 + \frac{T^2 e^{-2\eta\beta}}{1 - R^2 e^{-2\eta\beta}}\right], \tag{A.7}$$

$$P_t = P_0 \frac{T^2 e^{-\eta\beta}}{1 - R^2 e^{-2\eta\beta}}\ . \tag{A.8}$$

As mentioned before, the absorption factor β has contributions from band-to-band and free-carrier absorption and may be written as:

$$\beta = \alpha W + \alpha_{FCA} W\ , \tag{A.9}$$

where α and α_{FCA} are the band-to-band and average free-carrier absorption coefficient, respectively, and W is the wafer thickness.

Substituting Equation (A.9) into Equation (A.8*)*:

$$P_t = \frac{P_0 T^2 e^{-\eta\alpha W} e^{-\eta\alpha_{FCA} W}}{1 - R^2 e^{-2\eta\alpha W} e^{-2\eta\alpha_{FCA} W}}\ . \tag{A.10}$$

Letting $C = e^{-\eta\alpha W}$ and x $= \eta W \alpha_{FCA}$, the total transmitted power is given by:

$$P_t = \frac{P_0 T^2 C e^{-x}}{1 - R^2 C^2 e^{-2x}}\ . \tag{A.11}$$

The amplitude of the modulated term of the total transmitted power in the small signal limit, $P_{\mathrm{t,AC}}$,

can be determined by calculating its derivative with respect to x, as follows:

$$P_{t,AC} = \frac{dP_t}{dx}\Delta x = -P_0 T^2 A \frac{(1+R^2C^2)}{(1-R^2C^2)^2}\,\Delta x\,, \tag{A.12}$$

where $\Delta x = \eta W \Delta\alpha_{FCA}$. The FCA absorption is given by $\alpha_{FCA} = \sigma_{FCA} n$, where σ_{FCA} is the FCA cross-section and n is the mean excess carrier density induced by the pump laser. In the small signal limit, the FCA absorption can be defined as a time-dependent term: $\Delta\alpha_{FCA} = \sigma_{FCA}\Delta n_1$, where Δn_1 is the time-dependent excess carrier density of Equation (5.1).

Using $\Delta x = \eta W \Delta\alpha_{FCA} = \eta W \sigma_{FCA}\Delta n_1$ and taking into consideration that in the experiment the probe beam does not undergo band-to-band absorption ($\alpha = 0$) we can find $P_{t,AC}$:

$$P_{t,AC} = P_0 \frac{(1+R^2)}{(1+R)^2}\eta W \sigma_{FCA}\,\Delta n_1. \tag{A.13}$$

Similarly, the amplitude of the modulated term of the total reflected power can be calculated as:

$$P_{r,AC} = P_0 \frac{2R}{(1+R)^2}\eta W \sigma_{FCA}\Delta n_1\,. \tag{A.14}$$

I have included FCA photoabsorbance, i.e. the effects on the reflection and transmission coefficients due to changes in absorption from additional free carriers, but have neglected free carrier photoreflectance, i.e. the effects on the reflection and transmission coefficients due to changes in optical index from additional free carriers. It can be shown that the latter is much smaller than the former for our experimental configuration and so can be neglected. The Drude

model provides a simple framework to estimate these effects. Following Soref [65],

$$\Delta\alpha = \frac{q^3\lambda^2}{4\pi^2 c^3 \varepsilon_0 n}\left[\frac{n}{m_n^{*2}\mu_n} + \frac{p}{m_p^{*2}\mu_p}\right], \tag{A.15}$$

$$\Delta n = \frac{q^2\lambda^2}{8\pi^2 c^2 \varepsilon_0 n}\left[\frac{n}{m_n^{*}} + \frac{p}{m_p^{*}}\right], \tag{A.16}$$

where $\Delta\alpha$ and Δn are the magnitude of changes in absorption and index, respectively, induced by optical excitation. Here q is the fundamental electron charge, λ is the wavelength of light absorbed, ε_0 is the permittivity of free space, c is the speed of light, n is the refractive index of the semiconductor, m_n^* and m_p^* are the electron and hole conductivity effective masses, respectively, μ_n and μ_p are the electron and hole mobilities, respectively, and n and p are the concentrations of free electrons and holes, respectively. In this work, free electrons and holes are generated in a one-to-one ratio, so $n = p$. Using standard values for m_n^*, m_p^*, μ_n and μ_p for lightly-doped silicon, we find the ratio $W^* = \Delta n/\Delta\alpha \approx 21$ μm, independent of probe wavelength. Extending the methodology described in Equation (A.12), we can calculate the relative impact of index changes to absorption changes on the reflection and transmission terms. For normal incidence and $n \gg 1$, we find that the ratio of the index changes to absorption changes, upon optical carrier injection, is given by $4W^*/Wn^2$, for both reflection and transmission cases, where W is the sample thickness, as before. For $W = 575$ μm and using $n = 3.5$, we find a ratio of 0.012 for the sample under investigation and so we can safely neglect the effects of free carrier photoreflectance as compared to free carrier photoabsorbance. For very thin samples such that $W \ll W^*$, the opposite situation would occur.

Appendix B Calculation of the Ratio of the Modulated Amplitudes of the Reflected and Transmitted Powers for the Double-side Polished Sample

In the situation when the incident light has a mixed polarization, the power of the incident light can be represented by a combination of powers of two beams ($P_{0,\mathrm{s}} = P_0 \sin\theta$ and $P_{0,\mathrm{p}} = P_0 \cos\theta$, where θ represents the angle of polarization from 0 to 90 degrees) with two orthogonal polarizations (s and p). Therefore, the total reflected and transmitted powers in Equations (A.7), (A.8) can be divided into four equations with respect to s or p polarized light:

$$P_{r,s} = R_s P_{0,s}\left(1 + \frac{T_s^2 e^{-2\eta\beta}}{1 - R_s^2 e^{-2\eta\beta}}\right), \tag{B.17}$$

$$P_{r,p} = R_p P_{0,p}\left(1 + \frac{T_p^2 e^{-2\eta\beta}}{1 - R_p^2 e^{-2\eta\beta}}\right), \tag{B.18}$$

$$P_{t,s} = P_{0,s}\frac{T_s^2 e^{-\eta\beta}}{1 - R_s^2 e^{-2\eta\beta}}, \tag{B.19}$$

$$P_{t,p} = P_{0,p}\frac{T_p^2 e^{-\eta\beta}}{1 - R_p^2 e^{-2\eta\beta}}\ . \tag{B.20}$$

where R_s, R_p, T_s, and T_p are the reflection and transmission coefficients for s and p polarized light respectively. Next, using calculations made in Appendix A, we can transform Equations (B.17) - (B.20) into the amplitudes of the modulated terms of the total reflected and transmitted powers with respect to the polarization of the incident light:

$$P_{r,s,AC} = P_{0,s}T_s^2\frac{2R_s}{(1 - R_s^2)^2}\eta W\sigma_{FCA}\,\Delta n_1\ , \tag{B.21}$$

$$P_{r,p,AC} = P_{0,p}T_p^2\frac{2R_p}{\left(1 - R_p^2\right)^2}\,\eta W\sigma_{FCA}\,\Delta n_1, \tag{B.22}$$

$$P_{t,s,AC} = P_{0,s}T_s^2\frac{1 + R_s^2}{(1 - R_s^2)^2}\eta W\sigma_{FCA}\,\Delta n_1\ , \tag{B.23}$$

$$P_{t,p,AC} = P_{0,p}T_p^2\frac{1 + R_p^2}{\left(1 - R_p^2\right)^2}\eta W\sigma_{FCA}\,\Delta n_1\ . \tag{B.24}$$

The amplitudes of the modulated terms of the total reflected and transmitted powers consisting of both s and p polarized light can be calculated using Equations (B.21) - (B.24) and knowing that $P_r = \sqrt{P_{r,s}^2 + P_{r,p}^2}$ and $P_t = \sqrt{P_{t,s}^2 + P_{t,p}^2}$. Therefore:

$$P_{r,AC} = 2P_0\sigma_{FCA}\,\Delta n_1 \eta W \sqrt{\sin^2\theta \frac{T_s^4 R_s^2}{(1-R_s^2)^4} + \cos^2\theta \frac{T_p^4 R_p^2}{\left(1-R_p^2\right)^4}}\,, \tag{B.25}$$

$$P_{t,AC} = P_0\sigma_{FCA}\,\Delta n_1 \eta W \sqrt{\sin^2\theta \frac{T_s^4 (1+R_s^2)^2}{(1-R_s^2)^4} + \cos^2\theta \frac{T_p^4 \left(1+R_p^2\right)^2}{\left(1-R_p^2\right)^4}}\,. \tag{B.26}$$

Thus, the ratio $\mathcal{R}$ of the $P_{r,AC}$ and $P_{t,AC}$ is calculated as:

$$\mathcal{R} = \frac{P_{r,AC}}{P_{t,AC}} = 2\sqrt{\frac{R_S^2(1+R_P)^4\sin^2\theta + R_P^2(1+R_S)^4\cos^2\theta}{(1+R_S^2)^2(1+R_P)^4\sin^2\theta + (1+R_P^2)^2(1+R_S)^4\cos^2\theta}}\,. \tag{B.27}$$

Appendix C Calculation of the Amplitudes of the Modulated Terms of the Total Reflected and Transmitted Powers for the Double-side Textured Sample

When the light strikes an interface of a textured silicon sample, a fraction of the incident light is reflected and the rest is transmitted. If the textured surface has the same properties as the Lambertian surface, weakly absorbed light entering the surface gets scattered into different directions. As a result, the light rays become isotropically distributed inside the textured sample and the light forgets information about its initial direction. The total light that emerges from the front surface is the reflected light, while the total light that emerges from the back surface is the transmitted light.

The analysis presented here is similar to Appendix A – the total reflectance and transmittance of the sample are given by considering an infinite number of bounces, and the calculation procedure has the same logic. Performing the sums, the total reflection and transmission become:

$$P_r = P_0 \left[R_{tex} + (1 - R_{tex})^2 \frac{f(1-f')e^{-2Z\beta}}{1-(1-f')^2 e^{-2Z\beta}} \right] \tag{C.28}$$

$$P_t = P_0 (1 - R_{tex})^2 \frac{f e^{-Z\beta}}{1-(1-f')^2 e^{-2Z\beta}} \tag{C.29}$$

where $f' = \mathrm{f}(1 - \mathrm{R_{tex}})$, where f is the fraction of light that can escape from the medium at each interaction with the textured surface, which is determined by the critical angle of the total internal reflection. The fraction of light in the loss cone is given by: $f = 1/n^2$, where n is the refractive index of the medium. R_{tex} is the reflection coefficient of the textured surface, so the fraction of light that initially enters the wafer is equal to $(1 - R_{tex})$. Z is the ratio of the average traveling distance of the average light ray propagating from one surface to the other, relative to the wafer thickness.

Substituting Equation (A.9) into Equation (C.29):

$$P_t = P_0(1 - R_{tex})^2 \frac{f e^{-Z\alpha W} e^{-Z\alpha_{FCA} W}}{1 - (1 - f')^2 e^{-2Z\alpha W} e^{-2Z\alpha_{FCA} W}} \tag{C.30}$$

The fraction of the total absorbed power, which can be calculated as $A = 1 - P_r/P_0 - P_t/P_0$, is given by:

$$\mathrm{A} = 1 - R_{tex} - \left(1 + e^{-Z\alpha W} e^{-Z\alpha_{FCA} W}(1 - f')\right) \frac{f e^{-Z\alpha W} e^{-Z\alpha_{FCA} W}}{1 - (1 - f')^2 e^{-2Z\alpha W} e^{-2Z\alpha_{FCA} W}} \tag{C.31}$$

Simplifies to:

$$\mathrm{A} = 1 - R_{tex} - \frac{f(1 - R_{tex})^2 e^{-Z\alpha W} e^{-Z\alpha_{FCA} W}}{1 - (1 - f') e^{-Z\alpha W} e^{-Z\alpha_{FCA} W}} \tag{C.32}$$

The absorption coefficient formula derived above can be compared to the formula derived by Yablonovitch [29] for a double-side textured silicon wafer with no back reflector:

$$\mathrm{A} = \frac{2n^2\alpha W}{1 + 2n^2\alpha W} \tag{C.33}$$

where n is the refractive index of silicon. Equation (C.33) is applicable only for weakly absorbed light: $\alpha W \ll 1$, do not consider FCA: $\alpha_{FCA} W = 0$, and consider $R_{tex} = 0$. Z can be approximated by the average ray traveling distance equal to 2 times the device thickness [31], so $Z = 2$. With such assumptions Equation (C.31) can be rewritten:

$$\mathrm{A} = 1 - \left(1 + e^{-2\alpha W}(1 - f)\right)\frac{f e^{-2\alpha W}}{1 - (1 - f)^2 e^{-4\alpha W}} \tag{C.34}$$

which simplifies further to:

$$\mathrm{A} = 1 - \frac{f e^{-2\alpha W}}{1 - (1 - f)e^{-2\alpha W}} = \frac{1 - e^{-2\alpha W}}{1 - (1 - f)e^{-2\alpha W}} \tag{C.35}$$

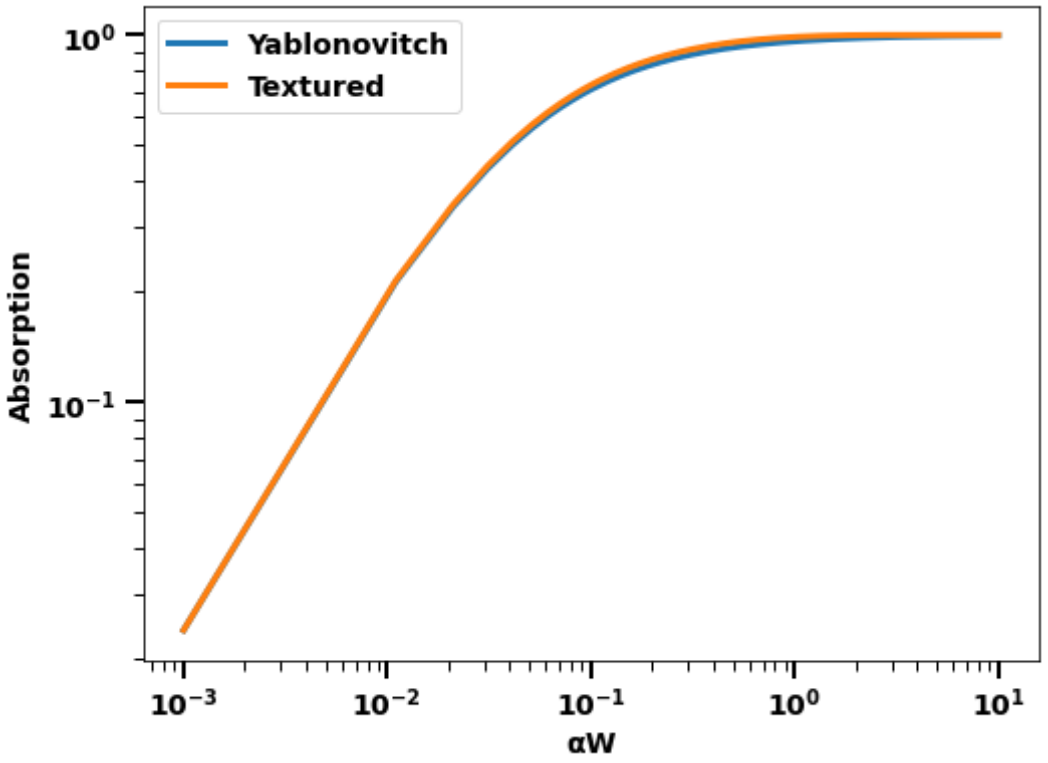

Figure 0.1. Absorption coefficient of a double-side textured silicon wafer versus αW calculated using Yablonovitch's formula and the Equation (C.34).

Figure 0.1. Absorption coefficient of a double-side textured silicon wafer versus αW calculated using Yablonovitch's formula and the Equation *(C.34)*.shows a comparison of an absorption coefficient derived using the Yablonovitch formula and the formula derived in this appendix. Equation (C.34) is in good agreement with the Yablonovitch formula especially for low values of αW. This means that the approach used in this work to describe the light propagation inside a textured silicon wafer give results consistent with Yablonovitch's results.

Letting $C = e^{-Z\alpha W}$ and $x = ZW\alpha_{FCA}$, the total transmitted power is given by:

$$P_t = P_0(1 - R_{tex})^2 \frac{fCe^{-x}}{1 - (1 - f')^2 C^2 e^{-2x}} \tag{C.36}$$

The amplitude of the modulated term of the total transmitted power in the small signal limit, $P_{t,AC}$, can be determined by calculating its derivative with respect to x, as follows:

$$P_{t,AC} = \frac{dP_t}{dx}\Delta x = -P_0(1-R_{tex})^2\frac{Cf(1+C^2(1-f')^2)}{(1-(1-f')^2C^2)^2}\Delta x, \tag{C.37}$$

where $\Delta x = ZW\Delta\alpha_{FCA}$. The FCA absorption is given by $\alpha_{FCA} = \sigma_{FCA}n$, where σ_{FCA} is the FCA cross-section and n is the mean excess carrier density induced by the pump laser. In the small signal limit, the FCA absorption can be defined as a time-dependent term: $\Delta\alpha_{FCA} = \sigma_{FCA}\Delta n_1$, where Δn_1 is the time-dependent excess carrier density of Equation (5.1).

Using $\Delta x = ZW\Delta\alpha_{FCA} = ZW\sigma_{FCA}\Delta n_1$ and taking into consideration that in the experiment the probe beam does not undergo band-to-band absorption ($\alpha = 0$) we can find $P_{t,AC}$:

$$P_{t,AC} = P_0(1-R_{tex})^2\frac{f(1+(1-f')^2)}{(1-(1-f')^2)^2}WZ\sigma_{FCA}\Delta n_1 \tag{C.38}$$

Similarly, the amplitude of the modulated term of the total reflected power can be calculated as:

$$P_{r,AC} = P_0(1-R_{tex})^2\frac{2f(1-f')}{(1-(1-f')^2)^2}\,WZ\sigma_{FCA}\Delta n_1 \tag{C.39}$$

Using assumption that f<<1, $P_{t,AC}$ and $P_{r,AC}$ can be simplified to:

$$P_{t,AC} = P_{r,AC} = \frac{(1-R_{tex})^2}{2f}P_0\,WZ\sigma_{FCA}\Delta n_1 \tag{C.40}$$

As stated before, Z can be approximated as 2, which leads to:

$$P_{t,AC} = P_{r,AC} = \frac{(1 - R_{tex})^2}{f} P_0 \, W \sigma_{FCA} \Delta n_1 \tag{C.41}$$

Appendix D Interference Effect in a Double-side Polished Silicon Wafer

The interference effect caused by multiple reflections of the probe beam inside a double-side polished silicon wafer can significantly impact the results of the MFCA experiment. This appendix examines in what conditions interference effects can occur in a polished silicon wafer. The main condition when interference occurs is when there is a strong overlap between the light beam passing through the sample and the consequent reflections of the beam inside the sample. It is assumed that most of the light escape the sample after two reflections. Therefore, an overlap between the transmitting beam and the first reflection of the beam from the back surface is considered. Figure 5.7 shows how the angle of incidence and the diameter of the incident beam affect the beam overlap percentage in a 575 mcm thick silicon wafer. In order to investigate this effect in more detail, I have completed a set of 2D FDTD simulations of light propagation inside a double-side polished silicon wafer for different thicknesses of the sample and different incident angles of the light beam.

Simulation results must be compared with theory to validate correctness of simulation. The reflectance of a double-side polished semiconductor in the air for a perpendicularly incident light is given by:

$$R = \frac{2a(1 - cosv)}{a + b - 2acosv} \tag{D.42}$$

where:

$$a = (1-n)^2(1+n)^2 \tag{D.43}$$

$$b = (1+n)^4 \tag{D.44}$$

$$v = \frac{4\pi nh}{\lambda_0} \tag{D.45}$$

Where n is the refractive index of the silicon wafer, h is the wafer's thickness, and λ_0 is the wavelength in vacuum.

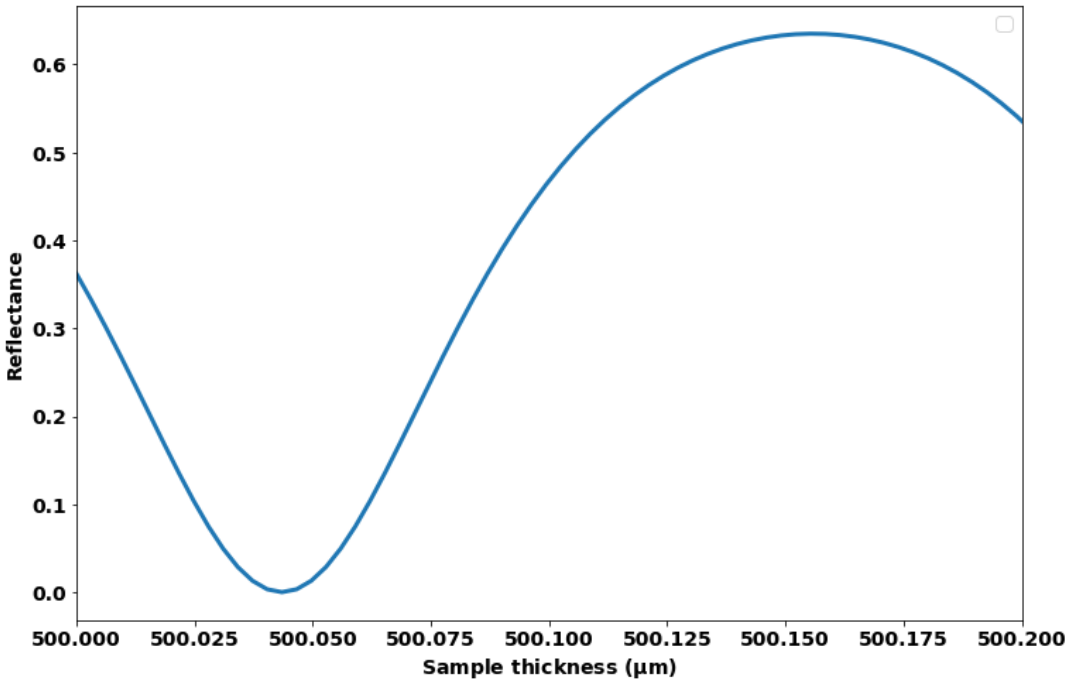

Figure 0.2. Reflectance of normally incident light from a double-side polished silicon sample versus sample's thickness.

Figure 0.2 shows how the reflectance of the double-side polished silicon sample changes when its thickness changes from 500 µm to 500.2 µm for a 1550 nm incident light. I have computed FDTD simulation where I analyzed how reflectance changes with changing sample's thickness.

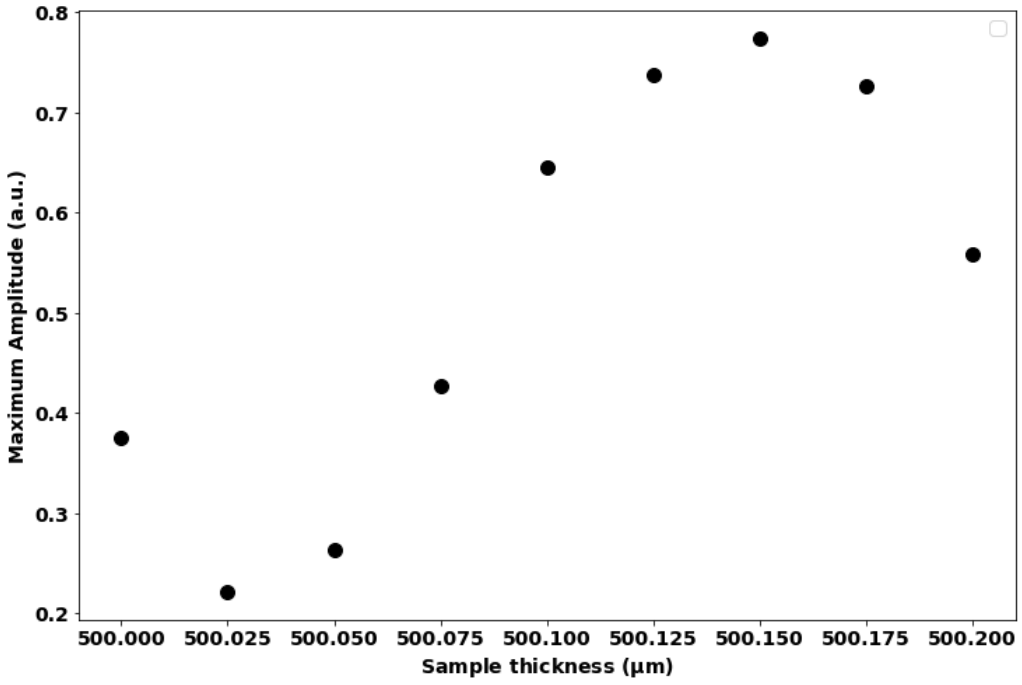

Figure 0.3. Reflectance of normally incident light from a double-side polished silicon sample versus sample's thickness calculated in FDTD simulation. Beam's diameter is equal to 50 µm.

Figure 0.3 presents the results of the FDTD simulation. It can be seen that the reflectance behavior is in good agreement with the theoretical model presented in Figure 0.2. The change in reflectance is caused by changes in interference pattern due to change in the sample's thickness. The difference in 200 nm causes a significant change in reflectance. Therefore, I assume that if the roughness of the sample's surface is in the range of 200 nm or higher, the interference pattern could average out and will not significantly affect the effective lifetime measurement results.

When the incident angle of the laser beam is about 45 degrees away from normal, the overlap between reflected beams inside the medium is relatively small (according to Figure 5.7) and interference effects do not occur. To prove this statement, I also computed FDTD simulations of 1550 nm light propagation in a 500 µm thick sample for a 45 degrees incident angle of the incoming beam.

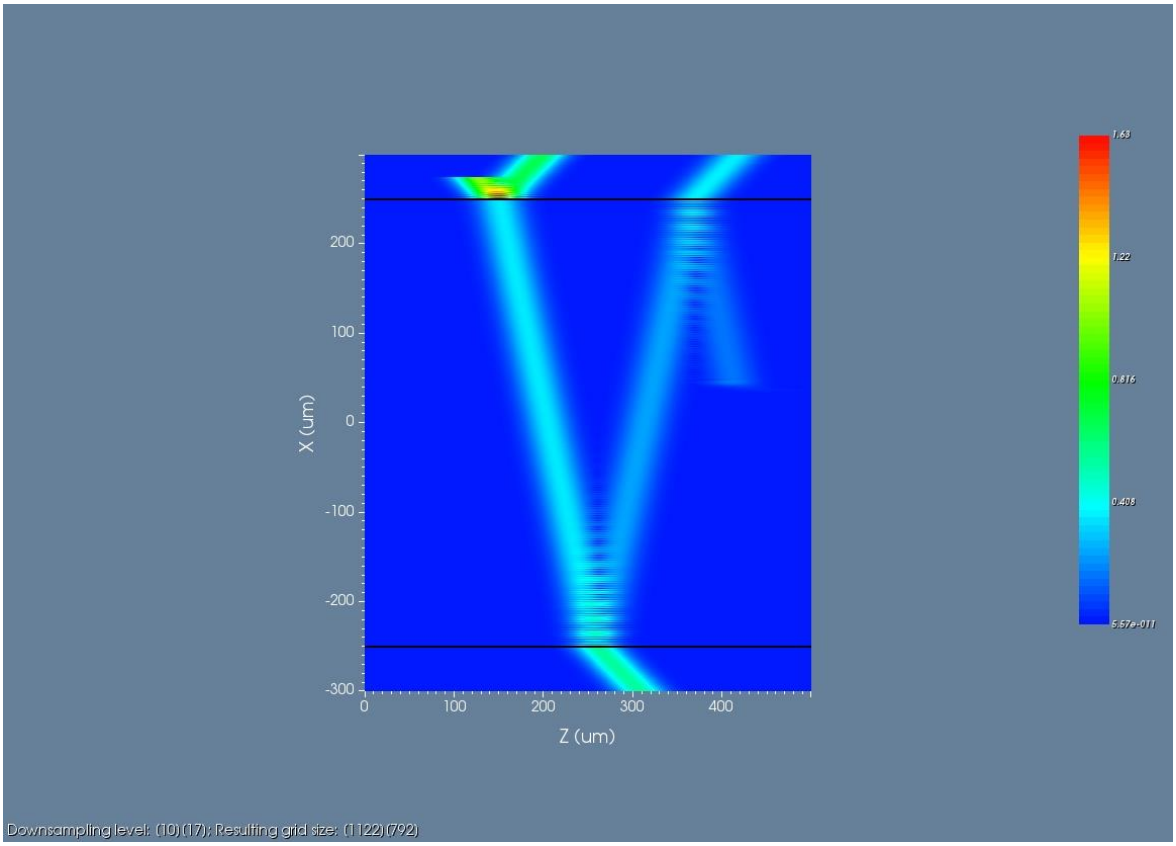

Figure 0.4. Cross section of FDTD simulation of light propagation inside a 500 μm thick silicon sample. Incident angle of the light beam is 45 degrees. Wavelength is 1550 nm. Beam's diameter is equal to 50 μm.

Figure 0.4 shows intensity of the propagated beam inside a silicon sample. Interference fringes occur near the edges of the sample where two beams overlap with each other. But the overlapping volume is much smaller compared to the full propagation volume of the beam. For this incident angle, I have done the same analysis of reflectance change versus change in thickness as for the case with a normal incident angle. If interference effects are strong for 45 degrees incident angle, total reflectance will change when the thickness of the sample changes.

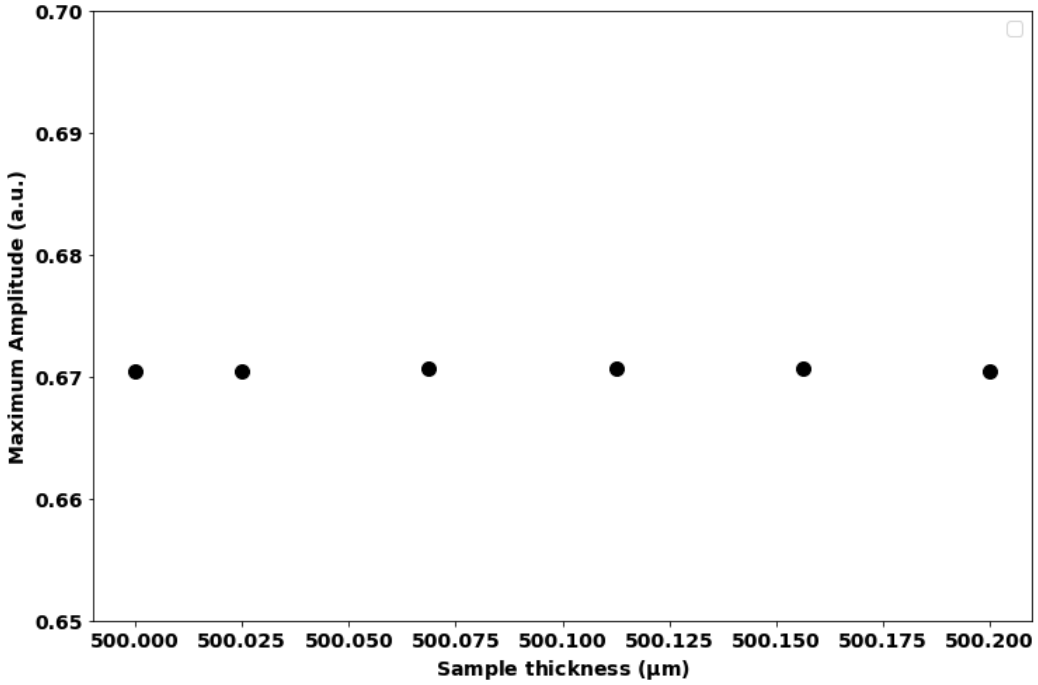

Figure 0.5. Reflectance of 45 degrees incident light from a double-side polished silicon sample versus sample's thickness calculated in FDTD simulation. Beam's diameter is equal to 50 µm.

Figure 0.5 shows that reflectance does not change with changing thickness for a 45 degrees incident angle. This means that at this angle interference effects can be neglected. Thus, incident angles that provide a relatively small overlap of the reflected beam inside the medium can be safely used for reflection and transmission mode MFCA measurements.